



1 Environmental changes during the onset of the Late Pliensbachian  
2 Event (Early Jurassic) in the Mochras Borehole, Cardigan Bay Basin,  
3 NW Wales.  
4

5 Teuntje P. Hollaar<sup>1,2</sup>, Stephen P. Hesselbo<sup>2,3</sup>, Jean-François Deconinck<sup>4</sup>, Magret Damaschke<sup>5</sup>,  
6 Clemens V. Ullmann<sup>2,3</sup>, Mengjie Jiang<sup>2</sup>, Claire M. Belcher<sup>1</sup>.

7 1 WildFIRE Lab, Global Systems Institute, University of Exeter, Exeter, EX4 4PS, UK

8 2 Camborne School of Mines, Department of Earth and Environmental Science, University of Exeter, Penryn  
9 Campus, Penryn, TR10 9FE, UK

10 3 Environment and Sustainability Institute, University of Exeter, Penryn Campus, Penryn, TR10 9FE, UK

11 4 Biogéosciences, UMR 6282 CNRS, Université de Bourgogne/Franche-Comté, 21000 Dijon, France

12 5 Core Scanning Facility, British Geological Survey, Keyworth, NG12 5GG, UK

13 Correspondence to: Teuntje P. Hollaar ([t.p.hollaar@exeter.ac.uk](mailto:t.p.hollaar@exeter.ac.uk))  
14

15 **Abstract.** The Late Pliensbachian Event (LPE), in the Early Jurassic, is associated with a perturbation in the  
16 global carbon cycle (positive carbon isotope excursion (CIE) of  $\sim 2$  ‰), cooling of  $\sim 5^\circ\text{C}$ , and the deposition of  
17 widespread regressive facies. Cooling during the Late Pliensbachian has been linked to enhanced organic matter  
18 burial and/or disruption of thermohaline ocean circulation due to North Sea doming. Orbital forcing had a strong  
19 influence on the Pliensbachian environments and recent studies show that the terrestrial realm and the marine  
20 realm in and around the Cardigan Bay Basin were strongly influenced by orbital climate forcing. In the present  
21 study we build on the previously published data for long eccentricity cycle  $E459 \pm 1$  and extend the  
22 palaeoenvironmental record to include  $E458 \pm 1$ . We explore the environmental and depositional changes on  
23 orbital time scales for the Mochras core during the onset of the LPE. Clay mineralogy, XRF elemental analysis,  
24 isotope ratio mass spectrometry, and palynology are combined to resolve systematic changes in erosion,  
25 weathering, fire, grain size and riverine influx. Our results indicate distinctively different environments before  
26 and after the onset of the LPE positive CIE, and show increased physical erosion relative to chemical  
27 weathering. We also identify 5 swings in the climate, in tandem with the 405 kyr eccentricity minima and  
28 maxima. Eccentricity maxima are linked to precessionally repeated occurrences of a semi-arid, monsoonal  
29 climate with high fire activity and relatively coarser fraction of terrestrial runoff. In contrast, 405 kyr minima in  
30 the Mochras core are linked to a more persistent, annually wet climate, low fire activity, and relatively finer  
31 grained deposits across multiple precession cycles. The onset of the LPE +ve CIE did not impact the expression  
32 of the 405 kyr in the proxy records, however, during the second pulse of lighter carbon ( $^{12}\text{C}$ ) enrichment, the  
33 clay minerals record a change from dominant chemical weathering to dominant physical erosion.

34

35 **1.1 Introduction**

36 The Early Jurassic is a period marked by large climatic fluctuations and associated carbon-isotope excursions  
37 (CIE's) in an overall warm and high  $p\text{CO}_2$  world (McElwain *et al.*, 2005; Korte & Hesselbo, 2011). A series of  
38 small and medium sized CIE's have recently been documented for the Sinemurian and Pliensbachian, which  
39 have mainly been recorded in European records (Korte & Hesselbo, 2011; Franceschi *et al.*, 2014; Korte *et al.*,



40 2015; Price *et al.*, 2016; Hesselbo *et al.*, 2020a; Storm *et al.*, 2020; Silva *et al.*, 2021; Cifer *et al.*, 2022) and  
41 recently at the NW end of the Tethys Ocean in Morocco (Mercuzot *et al.*, 2020) and in North America (De Lena  
42 *et al.*, 2019). Notable is the pronounced positive CIE in the Late Pliensbachian, which has been called the Late  
43 Pliensbachian Event (LPE) and is linked to climatic cooling (Hesselbo & Korte, 2011; Korte *et al.*, 2015) and a  
44 supra-regional/global sea level low stand (Hallam, 1981; de Graciansky *et al.*, 1998; Hesselbo & Jenkyns, 1998;  
45 Hesselbo, 2008). The LPE has been recognized by a positive shift in benthic marine oxygen-isotopes (~1.5–2  
46 per mil) (Bailey *et al.*, 2003; Rosales *et al.*, 2004,2006; Suan *et al.*, 2010; Dera *et al.*, 2011a; Korte & Hesselbo,  
47 2011; Gómez *et al.*, 2016; Alberti *et al.*, 2019, 2021), coeval with a positive shift in marine and terrestrial  
48 carbon isotopes (~2 per mil) (Jenkyns & Clayton, 1986; McArthur *et al.*, 2000; Morettini *et al.*, 2002; Quesada  
49 *et al.*, 2005; Rosales *et al.*, 2006; Suan *et al.*, 2010; Korte & Hesselbo, 2011; Silva *et al.*, 2011; Gómez *et al.*,  
50 2016; De Lena *et al.*, 2019).

51 A cooler Late Pliensbachian climate has been suggested based on low  $p\text{CO}_2$  values inferred by leaf stomatal  
52 index data from eastern Australia (Steinthorsdottir & Vajda, 2015), the presence of glendonites in northern  
53 Siberia (Kaplan, 1978; Price, 1999; Rogov & Zakharov, 2010), vegetation shifts from a diverse flora of different  
54 plant groups to one mainly dominated by bryophytes in Siberia (Ilyina, 1985; Zakharov *et al.*, 2006), and  
55 possible ice rafted debris found in Siberia (Price, 1999; Suan *et al.*, 2011). Whilst the presence of ice sheets is  
56 strongly debated, a general cooling period (~5°C lower; Korte *et al.*, 2015; Gómez *et al.*, 2016) is evident from  
57 several temperature reconstructions of NW Europe. A cooling is hypothesized via enhanced carbon burial in the  
58 marine sediments, leading to lower  $p\text{CO}_2$  values and initiating cooler climatic conditions (Jenkyns & Clayton,  
59 1986; Suan *et al.*, 2010; Silva *et al.*, 2011; Storm *et al.*, 2020). Direct evidence of large-scale carbon burial in  
60 Upper Pliensbachian marine deposits has not yet been documented (Silva *et al.*, 2021). Alternatively, cooling  
61 has been suggested to be caused by regional tectonic updoming of the North Sea region, which would have  
62 disrupted the ocean circulation in the Laurasian Seaway, reducing poleward heat transport from the tropics  
63 (Korte *et al.*, 2015). Disruption of the ocean circulation between the western Tethys and the Boreal realm is  
64 supported by marine migration patterns (Schweigert, 2005; Zakharov *et al.*, 2006; Bourillot *et al.*, 2008;  
65 Nikitenko, 2008; Dera *et al.*, 2011b; van de Schootbrugge *et al.*, 2019) and numerical models (Bjerrum *et al.*,  
66 2001; Dera & Donnadieu, 2012; Ruvalcaba Baroni *et al.* 2018); however, the direction of the flows remain  
67 debated.

68 An additional factor at this time is that a strong orbital control exists on the sedimentary successions in the  
69 Pliensbachian (Weedon & Jenkyns, 1990; Ruhl *et al.*, 2016; Hinnov *et al.*, 2018; Storm *et al.*, 2020; Hollaar *et al.*,  
70 *et al.*, 2021). Previous studies have indicated that sea level changes, possibly coupled to glacio-eustatic rise and  
71 fall, occurred during the LPE on a 100 kyr (short eccentricity) time scale (Korte & Hesselbo, 2011). A high-  
72 resolution record of charcoal, clay mineralogy, bulk-organic carbon-isotopes, TOC and  $\text{CaCO}_3$  encompassing  
73 approximately one 405 kyr cycle from the Llanbedr (Mochras Farm) borehole, Cardigan Bay Basin, NW Wales,  
74 UK suggested that the long-eccentricity orbital cycle had a significant effect on background climatic and  
75 environmental change at this time, particularly affecting the hydrological regime of the region (Hollaar *et al.*,  
76 2021). This previous research focussed on orbital forcing of environmental change for a time lacking any large  
77 excursion in  $\delta^{13}\text{C}_{\text{org}}$ , and so unaffected by perturbations to the global carbon cycle. Here, we expand on the  
78 record of Hollaar *et al.* (2021) to cover two long eccentricity cycles (which we identify as cycle  $\text{E}459 \pm 1$  and



79 E458 ± 1 of Laskar *et al.* 2011), where the final parts of E458 and the start of E457 are interrupted by onset of  
80 the Late Pliensbachian Event. We find that the long eccentricity forcing continued to dictate the precise timing  
81 of major environmental changes in the Cardigan Bay Basin, including the initial step of the positive carbon  
82 isotope excursion.

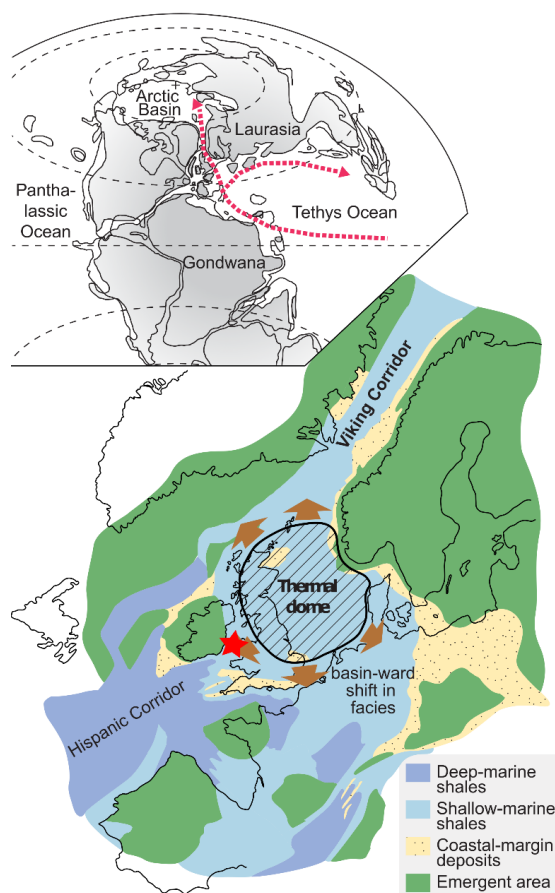
83

## 84 1.2 Material

### 85 1.2.1 Palaeo-location and setting

86 Associated with the break-up of Pangea, connections between oceans via epicontinental seaways were  
87 established during the Early Jurassic, such as the Hispanic Corridor, which connected the north-western Tethys  
88 and the eastern Panthalassa, and the Viking Corridor which linked the north-western Tethys Ocean to the Boreal  
89 Sea (Sellwood & Jenkyns, 1975; Smith *et al.*, 1983; Bjerrum *et al.*, 2001; Damborenea *et al.*, 2012). The linking  
90 passage of the NW Tethys Ocean and the Boreal Sea (south of the Viking Corridor) is the palaeogeographical  
91 location of the Llanbedr (Mochras Farm) borehole, Cardigan Bay Basin, NW Wales, UK (Fig. 1) – referred to  
92 hereafter as Mochras. Due to the location of the Mochras succession during the Late Pliensbachian, it was  
93 subject to both polar and equatorial influences allowing the study of variations in the circulation in the N-S  
94 Laurasian Seaway (including the Viking Corridor) prior to and across the LPE. Mochras was located at a mid-  
95 palaeolatitude of ~35° N (Torsvik & Cocks, 2017).

96



97

98 **Figure 1: Palaeolocation of the Mochras borehole in the context of potential North Sea doming.** Figure  
99 reprinted and adapted from Korte *et al.* (2015), which is open access  
100 (<https://creativecommons.org/licenses/by/4.0/>). The Mochras borehole was located at a paleolatitude of ~35° N  
101 in the Cardigan Bay Basin (Torsvik & Cocks, 2017). Circulation in the Tethys Ocean and between there and the  
102 Boreal region influenced the depositional environment of the Mochras core (Pieńkowski *et al.*, 2021). Late  
103 Pliensbachian uplift of the North Sea dome potentially led to occlusion of the Viking Corridor and disrupted  
104 circulation in the seaway (Korte *et al.*, 2015).

105

106 The depositional environment of Mochras is likely characterized by a rift setting, which is reflected by the  
107 relatively open and deep marine facies and the evidence for below storm wave-base and contourite deposition  
108 (Pieńkowski *et al.*, 2021), but always with a strong terrestrial influence (van de Schootbrugge *et al.*, 2005;  
109 Riding *et al.*, 2013) from the nearby landmasses (Dobson & Whittington, 1987). The Cardigan Bay Basin fill  
110 was downthrown against the Early Paleozoic Welsh Massif on the SE side by a major normal fault system,  
111 probably comprising the Bala, Mochras and Tonfanau faults at the eastern and south-eastern margins of the  
112 basin in Late Paleozoic–Early Mesozoic time (Woodland, 1971; Tappin *et al.*, 1994). The main source of



113 detrital material is understood to be the Welsh Massif, followed by the Irish Massif (Deconinck *et al.*, 2019).  
114 Other Variscan massifs that could have influenced the provenance are the London-Brabant Massif to the south  
115 east, and Cornubia to the south (van de Schootbrugge *et al.*, 2005), depending on the marine circulation and  
116 sediment transport at the time.

### 117 1.2.2 Core location and material

118 The Llanbedr (Mochras Farm) Borehole was drilled onshore in the Cardigan Bay Basin (52°48'32"N, 4°08'  
119 44"W) in 1967–1969, North Wales (Woodland, 1971; Hesselbo *et al.*, 2013). The borehole recovered a 1300 m  
120 thick Early Jurassic sequence (601.83 – 1906.78 metres below surface (mbs)), yielding the most complete and  
121 extended Early Jurassic succession in the UK, being double the thickness of same age strata in other UK cores  
122 and outcrops (Hesselbo *et al.*, 2013; Ruhl *et al.*, 2016). The Lower Jurassic is biostratigraphically complete at  
123 the zonal level (Ivimey-Cook, 1971; Copestake & Johnson, 2014), with the top truncated and unconformably  
124 overlain by Cenozoic strata (Woodland, 1971; Dobson & Whittington, 1987; Tappin *et al.*, 1994; Hesselbo *et al.*,  
125 2013). The lithology is dominated by argillaceous sediments, with alternating muddy limestone, marl and  
126 mudstone (Woodland, 1971; Sellwood & Jenkyns, 1975).

### 127 1.2.3 Pliensbachian

128 The Pliensbachian Stage in the Mochras borehole occurs between ~865 to ~1250 mbs, with the Margaritatus  
129 Zone between ~1013 and 909 mbs (Page in Copestake & Johnson, 2014). The Pliensbachian interval comprises  
130 alternations of mudstone (with a relatively moderate total organic carbon [TOC]) and organic poor limestones,  
131 with a pronounced cyclicity at  $\sim 1 \pm 0.5$  m wavelength (Ruhl *et al.*, 2016). The Upper Pliensbachian contains  
132 intervals that are silty and locally sandy, whilst levels of relative organic enrichment also occur through the  
133 Pliensbachian (Ruhl *et al.*, 2016). Overall, the Upper Pliensbachian is relatively rich in carbonate (Ruhl *et al.*,  
134 2016; Ullmann *et al.*, 2022).

135

### 136 1.3 Methods

137 For this study, samples were taken at a ~30 cm resolution from slabbed core from 918–934 mbs for XRD and  
138 mass spectrometry, as well as palynofacies and microcharcoal analysis. These new samples complement a set at  
139 10 cm resolution from 951–934 mbs (results published in Hollaar *et al.*, 2021).

#### 140 1.3.1 TOC, CaCO<sub>3</sub> and bulk organic carbon isotope mass spectrometry

141 TOC and  $\delta^{13}\text{C}_{\text{org}}$  were measured to track the changes in the total organic fraction and the bulk organic carbon  
142 isotope ratios simultaneously with the other palaeoenvironmental proxy data.

143 Powdered bulk-rock samples (~2 g) were decarbonated in 50 ml of 3.3% HCl. After this, the samples were  
144 transferred to a hot bath of 79 °C for 1 h to remove siderite and dolomite. Subsequently, the samples were  
145 centrifuged and the liquid decanted. The samples were rinsed repeatedly with distilled water to reach neutral pH.  
146 After this, the samples were oven-dried at 40 °C, re-powdered and weighed into tin capsules for mass  
147 spectrometry with the Sercon Integra 2 stable isotope analyser at the University of Exeter Environmental &  
148 Sustainability Institute (ESI), stable isotope facility on the Penryn Campus, Cornwall. Samples were run  
149 alongside in house reference material (bovine liver;  $\delta^{13}\text{C}$  -28.61 and Alanine;  $\delta^{13}\text{C}$  -19.62) which was used to  
150 correct for instrument drift and to determine the  $\delta^{13}\text{C}$  values of the samples.  $\delta^{13}\text{C}_{\text{org}}$  values reported relative to V-



151 PDB following a within-run laboratory standard calibration. Total organic carbon was determined using the CO<sub>2</sub>  
152 beam area relative to the bovine liver standard (%C 47.24). Replicate analysis of the in-house standards gave a  
153 precision of  $\pm <0.1$  ‰ (2 SD).

154 The carbonate content was measured by the dry weight sample loss before and after decarbonation. The %C  
155 content derived from the mass spectrometer was corrected for carbonate loss to derive TOC.

### 156 **1.3.2 X-Ray Diffraction (XRD) to determine clay mineralogy**

157 Clay mineral analysis was performed to gain insight into the relative importance of physical erosion versus  
158 chemical weathering and related changes in the hydrological cycle.

159 About 2–3 g of gently powdered bulk-rock was decarbonated with a 0.2 M HCl solution and the clay sized  
160 fraction ( $< 2$   $\mu\text{m}$ ) extracted and oriented on glass slides for X-ray diffraction analysis (XRD) using a Bruker D4  
161 Endeavour diffractometer (Bruker, Billerica, MA, USA) with Cu K $\alpha$  radiations, LynxEye detector and Ni filter  
162 under 40 kV voltage and 25 mA intensity (Biogéosciences Laboratory, Université Bourgogne/Franche-Comté,  
163 Dijon). Following Moore & Reynolds (1997), the clay phases were discriminated in three runs per sample: (1)  
164 air-drying at room temperature; (2) ethylene-glycol solvation during 24 h under vacuum; (3) heating at 490 °C  
165 during 2 h.

166 Identification of the clay minerals was based on their main diffraction peaks and by comparing the three  
167 diffractograms obtained. The proportion of each clay mineral on glycolated diffractograms was measured using  
168 the MACDIFF 4.2.5. software (Petschick, 2000). Identification of the clay minerals follows the methods in  
169 Deconinck *et al.* (2019) and Moore & Reynolds (1997).

### 170 **1.3.3 Palynofacies and microcharcoal**

171 Palynofacies were examined to explore shifts in the terrestrial versus marine origin of the particulate organic  
172 matter. Each ~ 20 g bulk rock sample was split into 0.5 cm<sup>3</sup> fragments, minimizing breakage of charcoal and  
173 other particles, to optimize the surface area for extraction of organic matter using a palynological acid  
174 maceration technique. The samples were first treated with cold hydrochloric acid (10% and 37% HCl) to remove  
175 carbonates. Following, hydrofluoric acid (40% HF) was added to the samples to remove silicates. Carbonate  
176 precipitation was prevented, by adding cold concentrated HCl (37%) after 48 h. The samples were neutralized  
177 via multiple DI water dilution-settling-decanting cycles, after which 5 droplets of the mixed residue were taken  
178 for the analysis of palynofacies prior to sieving. The remaining residue was sieved through a 125  $\mu\text{m}$  and 10  $\mu\text{m}$   
179 mesh to extract the microcharcoal fraction.

180 A known quantity (125  $\mu\text{l}$ ) of the 10–125  $\mu\text{m}$  sieved residue was mounted onto a palynological slide using  
181 glycerine jelly. This fraction, containing the microscopic charcoal, was analysed and the charcoal particles  
182 counted using an Olympus (BX53) transmitted light microscope (40x10 magnification). For each palynological  
183 slide four transects (two transects in the middle and one on the left and right side of the coverslip) were followed  
184 and the number of charcoal particles determined. Charcoal particles were identified with the following criteria:  
185 opaque and black, often elongated lath-like shape with sharp edges, original anatomy preserved, brittle  
186 appearance with a lustrous shine (Scott, 2010). These data were then scaled up to the known quantity of the  
187 sample according the method of Belcher *et al.* (2005).



188 Palynofacies were grouped broadly according to Oboh-Ikuenobe *et al.* (2005): sporomorphs, fungal remains,  
189 freshwater algae, marine palynomorphs, structured phytoclasts, unstructured phytoclasts, black debris,  
190 amorphous organic matter (AOM), and charcoal (further described in Hollaar *et al.*, 2021). The palynofacies  
191 were quantified on a palynological slide using the optical light microscope (40x10 magnification) and counting  
192 a minimum of 300 particles per slide. Because the samples are AOM-dominated, counting was continued until a  
193 minimum of 100 non-AOM particles were observed. We used the percentage of terrestrial phytoclasts, which  
194 includes sporomorphs, structured and unstructured phytoclasts, to examine changes in terrestrial organic particle  
195 content.

196

#### 197 **1.3.4 X-Ray Fluorescence (XRF) to determine detrital elements**

198 Detrital elemental ratios were examined to analyse changes in relative terrestrial influx and the type of material  
199 transported from the land to the marine realm. The slabbed archive halves of the Mochras borehole were  
200 scanned via automated X-ray fluorescence (XRF) at a 1 cm resolution for the interval 951 – 918 mbs, with the  
201 ITRAX MC at the British Geological Survey Core Scanning Facility (CSF), Keyworth, UK (Damaschke *et al.*,  
202 2021). The measurement window was 10 s and long-term drift in the measurement values was counteracted by  
203 regular internal calibration with a glass reference (NIST-610). Duplicate measurements were taken every 5 m  
204 for a 50 cm interval to additionally verify the measured results.

#### 205 **1.3.5 Statistical analysis**

206 Principal component analysis (PCA) was performed in the software PAST on the normalized dataset including  
207 microcharcoal, TOC, CaCO<sub>3</sub>, δ<sup>13</sup>C<sub>org</sub>, S/I, K/I, primary clay mineralogy, Si/Al, Zr/Rb. The samples before the  
208 +ve CIE (951.0–930.4 mbs) and the samples after the +ve CIE (930.3–918.0 mbs) are grouped to examine a  
209 potential difference in the sedimentary composition before and after the +ve CIE.

210 A Pearson's correlation was executed in Matlab R2017b. The *p* value tests the hypothesis of no correlation  
211 against the alternative hypothesis of a positive or negative correlation (significance level at  $p \leq 0.05$ ).

212

### 213 **1.4 Results**

214

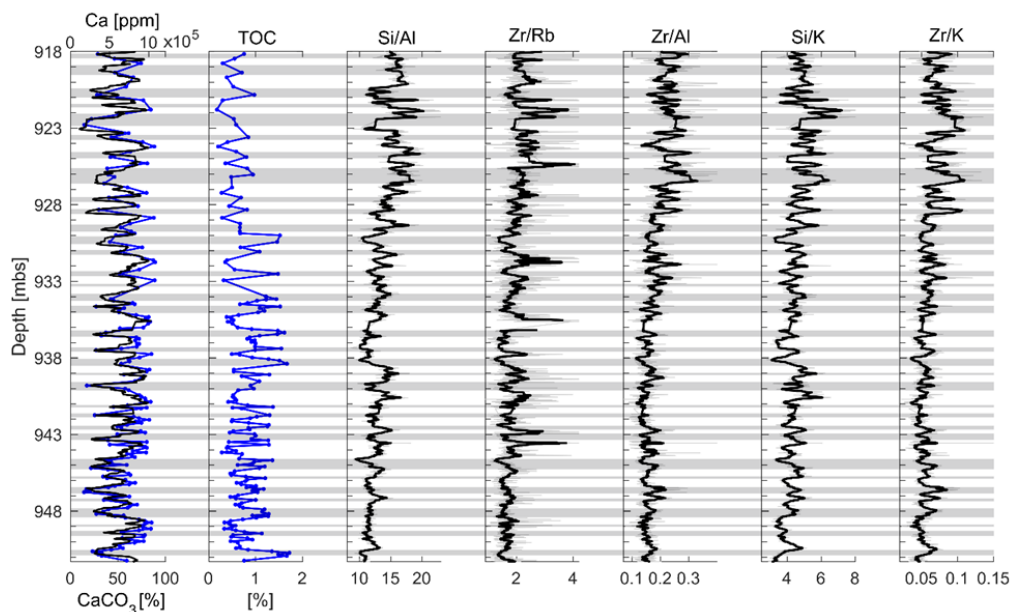
#### 215 **1.4.1 TOC, CaCO<sub>3</sub> and bulk organic carbon isotope ratio mass spectrometry**

216 Alternating TOC-enhanced and Ca-rich lithological couplets occur on a metre scale through the studied interval  
217 ( $r = -0.64$ ,  $p = 0.001$ ). TOC content fluctuates in the range 0.17–1.72 wt% (mean 0.8 wt%) and the highest  
218 fluctuations of TOC content are found from 939–930 mbs. The CaCO<sub>3</sub> content fluctuates in opposition of TOC  
219 and varies between 14 and 89 %. The studied interval is generally high in CaCO<sub>3</sub> (mean 58 %) (Fig. 2). The  
220 δ<sup>13</sup>C<sub>org</sub> displays a minor (~0.5 ‰) shift towards more positive values at ~944 mbs (as reported in Storm *et al.*,  
221 2020; Hollaar *et al.*, 2021). At ~930 mbs an abrupt shift of ~1.8 ‰ (Fig. 3 and 4; Storm *et al.*, 2020) indicates  
222 the onset of the Late Pliensbachian Event (LPE) in the Mochras core. In agreement with this, the results of the  
223 present study show a shift from ~ minus 27 per mil to ~ minus 25.15 per mil between 930.8 and 930.4 mbs (Fig.  
224 3). The δ<sup>13</sup>C<sub>org</sub> data presented here have been divided into three phases: the pre-LPE gradual rise, followed by  
225 the +ve CIE, which is subdivided into pulses 1, 2 and 3 (Fig. 4). After the onset of the positive δ<sup>13</sup>C<sub>org</sub> excursion,  
226 the TOC content drops to the lowest values (from 0.85 % before and 0.6 % after the +ve CIE on average), but



227 the 1 metre fluctuations continue (Fig. 2 and Fig. 3). No overall change in the  $\text{CaCO}_3$  content is observed  
228 through the positive carbon-isotope excursion (Fig. 2).

229



230

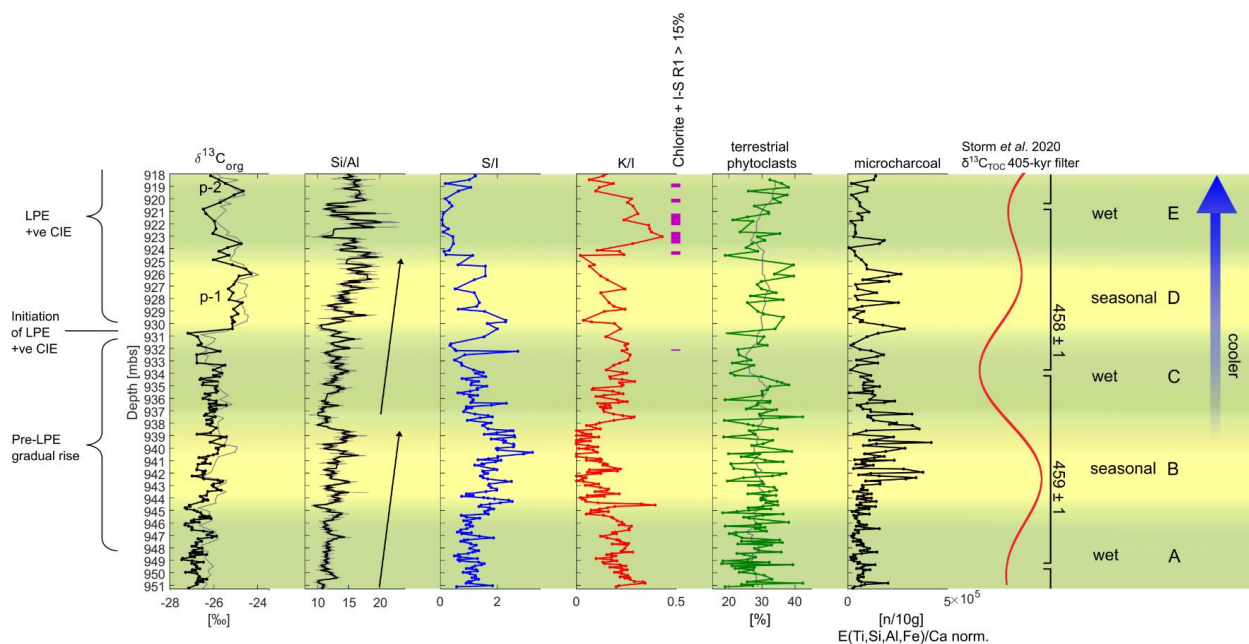
231 **Figure 2: Detrital ratios over the lithological Ca-rich and TOC-enhanced couplets for the studied**  
232 **interval.** Overview of Ca (black, derived from Ruhl *et al.* 2016),  $\text{CaCO}_3$  (blue), and TOC content of the studied  
233 interval 951–918 mbs. The grey shading represents the TOC-enhanced lithological beds and the unshaded bands  
234 mark the Ca-rich (limestone) beds. The detrital ratios reflect the silt to fine sand fraction (Si, Zr) versus the clay  
235 fraction (Rb, Al, K). Two increasing upward cycles are observed in the Si/Al and Zr/Rb ratios. The pattern  
236 observed in all detrital ratios (except the Ti/Al) is similar and likely reflects changes in grain size.

237

#### 238 1.4.2 Clay minerals

239 XRD analysis shows that the main clay types found in this interval are illite, random illite-smectite mixed-layers  
240 (I-S R0) [hereafter referred to as smectite], and kaolinite. Illite and kaolinite co-fluctuate in the interval studied  
241 here, and are directly out of phase with smectite abundance. Chlorite and R1 I-S are present in minor  
242 proportions, but reach sporadically higher relative abundance (> 10 %) from ~ 932 mbs upwards, with sustained  
243 >10% abundance at ~925–918 mbs (Fig. 3 and SI Fig. 1). The relative abundances of smectite and illite and of  
244 kaolinite and illite are expressed by the ratio S/I and K/I respectively. These ratios were calculated according to  
245 the intensity of the main diffraction peak of each mineral.

246



247

248 **Figure 3: Synthesis diagram showing the climatic swings observed in tandem with the long eccentricity**  
 249 **cycle.** The studied interval comprises part of the pre LPE gradual rise, the initiation of the LPE +ve CIE and  
 250 pulse 1 and 2. Five climatic phases (A–E) are interpreted from the Si/Al, smectite/illite, kaolinite/illite, chlorite  
 251 and I-S R1 abundance and the microcharcoal abundance. In tandem with the 405 kyr cycle (Storm *et al.*, 2020)  
 252 climatic state of a year-round wet climate, low fire activity and fine-grained sediments across multiple  
 253 precession cycles (phase A and C) alternates with a climatic state that includes repeated precessionally driven  
 254 states that are semi-arid, with high fire activity and coarser sediments (phase B and D). The top of the record  
 255 (phase E) indicates increased physical erosion (chlorite + I-S R1, kaolinite) relative to chemical weathering.

256

257

258

259

260

261

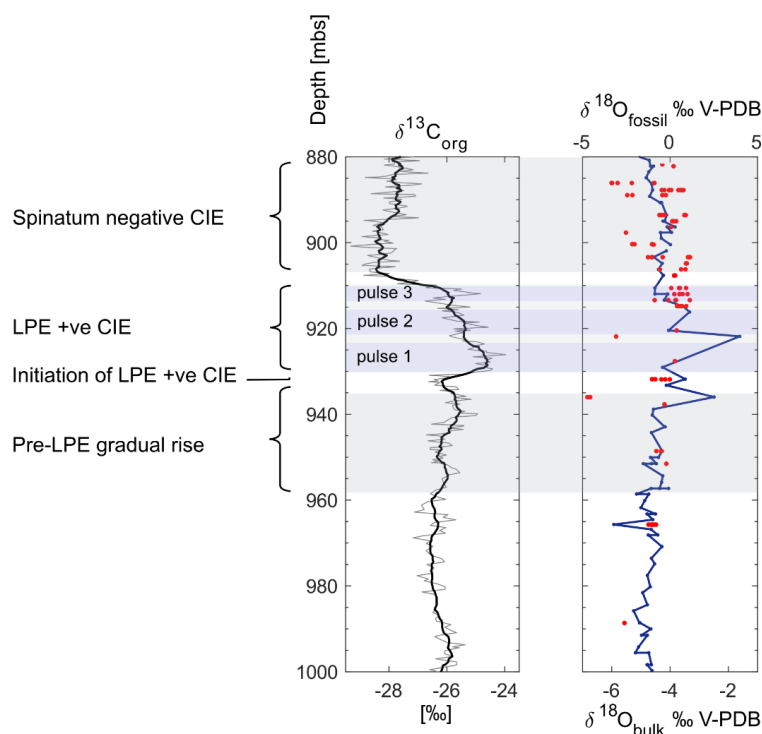
262

263

264



265



266

267 **Figure 4: The  $\delta^{13}\text{C}_{\text{org}}$  (Storm *et al.*, 2020) and  $\delta^{18}\text{O}_{\text{bulk}}$  and  $\delta^{18}\text{O}_{\text{fossil}}$  (Ullmann *et al.*, 2022) from the Late**  
268 **Pliensbachian of the Mochras core.** A pre-LPE gradual rise is recorded in the  $\delta^{13}\text{C}_{\text{org}}$  of the Mochras core,  
269 followed by the initiation of the LPE +ve CIE, which consists of three pulses. After the LPE +ve CIE,  $\delta^{13}\text{C}_{\text{org}}$   
270 values drop and the Spinatum negative CIE is recorded. The  $\delta^{18}\text{O}_{\text{bulk}}$  of the Mochras core (blue) are  
271 diagenetically altered and are unlikely to preserve a palaeoclimatic imprint (Ullman *et al.*, 2022); however, peak  
272 values in the  $\delta^{18}\text{O}_{\text{bulk}}$  occur during the LPE +ve CIE. Also, the  $\delta^{18}\text{O}_{\text{fossil}}$  values (red) are slightly more positive  
273 during pulse 3 of the LPE +ve CIE.

274

### 275 1.4.3 Organic matter

276 The type of particulate organic matter, and more specifically the abundance in the either marine or terrestrial  
277 origin of the particles, fluctuate on a metre scale from 18–42 %. Palynofacies indicate that the type of organic  
278 matter does not change in relation to the metre-scale lithological facies cycles (no correlation between  
279 percentage terrestrial phytoclasts and TOC or  $\text{CaCO}_3$ ). The proportion of terrestrial phytoclasts increases  
280 towards the top of the record and has 4 high phases: between 944.6 and 942.0 mbs, 937.5 and 934.9 mbs, 930.4  
281 and 925.4 mbs, and 920.3 and 918.0 mbs (SI Fig. 2). The first and second high phase falls within the + 0.5 ‰  
282 positive swing in the  $\delta^{13}\text{C}_{\text{org}}$ ; the latter two high phases correspond to pulse 1 and pulse 2 in the +ve CIE.



283 Amorphous organic matter (AOM) is very abundant, followed by unstructured phytoclasts, with lower  
284 proportions of structured phytoclasts and charcoal (SI Fig. 3). Microcharcoal particles make up a relatively large  
285 proportion of the terrestrial particulate organic matter (~10 % on average) and ~3.5 % on average of the total  
286 particulate organic matter fraction (SI Fig. 3). Only sparse marine and terrestrial palynomorphs were observed  
287 (SI Fig. 3). No abrupt changes are recorded in the terrestrial/marine proportions, but small long-term  
288 fluctuations are observed in the percentage of terrestrial phytoclasts, with three phases of increase noted, of  
289 which the overall highest phase occurs after the start of the +ve CIE.

290 To assess the character of the observed fluctuations in charcoal abundance, whether changes in charcoal can be  
291 related to enhanced runoff from the land and/or organic preservation, or if the charcoal signifies changes in fire  
292 activity on land, the charcoal record was corrected for detrital influx. We adjust the charcoal particle abundances  
293 using the XRF elemental record, normalizing to the total terrigenous influx following Daniau *et al.* (2013) and  
294 Hollaar *et al.* (2021). The stratigraphic trends in the normalized microcharcoal for  $E_{ter}/Ca$ ,  $Si/Al$ ,  $Ti/Al$  and  
295  $Fe/Al$  remain the same (SI Fig. 4). The absolute number of charcoal particles decreases, with raw mean charcoal  
296 particles  $1.06 \times 10^5$  per 10 g and  $E_{ter}/Ca$  normalized mean  $9.7 \times 10^4$  n/10g,  $Ti/Al$  normalized  $6.4 \times 10^4$  n/10g,  $Si/Al$   
297 normalized  $7.7 \times 10^4$  n/10g,  $Fe/Al$  normalized  $9.8 \times 10^4$  mean number of microcharcoal particles per 10 g (SI Fig.  
298 4). The number of charcoal particles per 10 g processed rock decreases when correcting for terrestrial run-off  
299 changes, hinting that perhaps part of the ‘background’ charcoal is related to terrestrial influx; the normalisation  
300 also shows that the observed patterns in charcoal abundances are not influenced by changes in terrestrial runoff  
301 and taphonomy. Hence, the highs and lows in the charcoal record can be interpreted to represent changes in the  
302 fire regime on land. The microcharcoal abundance fluctuates strongly in the record presented here; however, no  
303 clear difference in charcoal content has been observed before and after the onset of the +ve CIE.

304

#### 305 1.4.4 Detrital elemental ratios (XRF)

306 Strong similarities are observed between the fluctuating ratios of  $Si/Al$ ,  $Si/K$ ,  $Zr/Rb$ ,  $Zr/Al$  and  $Zr/K$  (Fig. 2).  
307 The elements Al, Rb and K sit in the clay fraction (e.g. Calvert & Pederson, 2007), whereas Si and Zr are often  
308 found in the coarser fraction related to silt and sand grade quartz and heavy minerals (Calvert & Pederson,  
309 2007). The ratios all show clear metre-scale fluctuations, and these are superimposed on two increasing-upward  
310 trends observed in both the  $Si/Al$  and the  $Zr/Rb$ , followed by a drop and rise to peak values in the latest part of  
311 phase D and phase E above the onset of the +ve CIE (Fig. 2; Fig. 3). A parallel trend is observed between the  
312 clay ratios (XRD) and elemental ratios  $Si/Al$  and  $Zr/Rb$  (Fig. 2). Phases of high  $S/I$  correspond to the peaks in  
313 the two coarsening upward sequences, whereas phases of high  $K/I$  correspond to the low phases in the two  
314 coarsening upward sequences. After the +ve CIE onset (in phase E) this relationship turns around, and an  
315 enrichment in the kaolinite/illite ratio corresponds to the elemental ratios, where highest kaolinite relative  
316 abundance is observed in parallel with elemental ratios suggesting maximum coarse fraction.

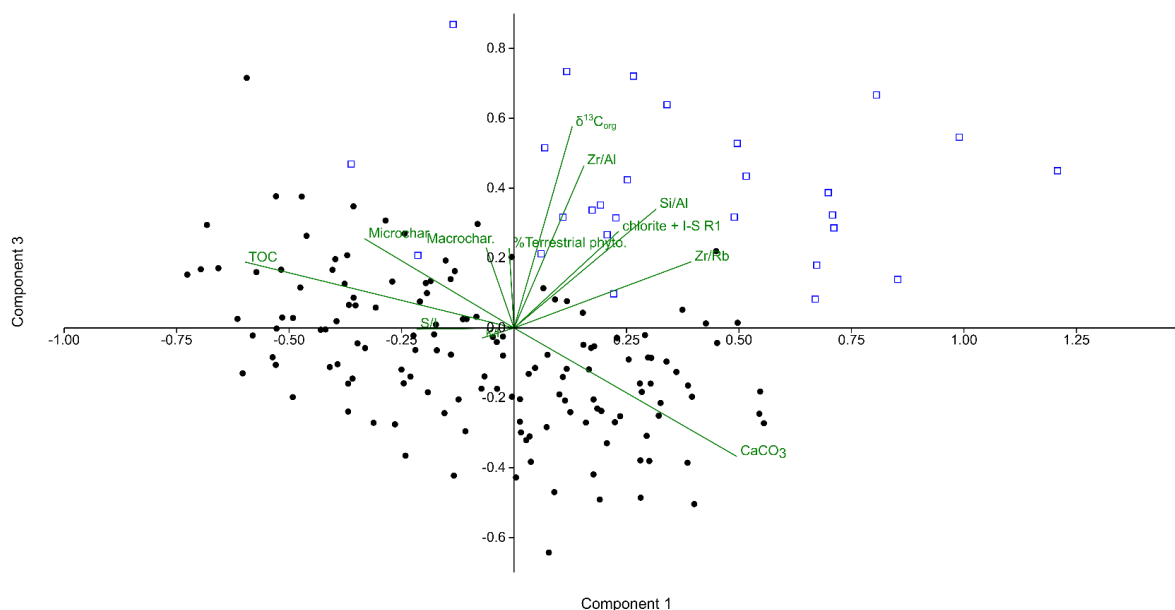
317

#### 318 1.4.5 PCA analysis

319 The proxy datasets ( $\delta^{13}C_{org}$ , TOC, percentage terrestrial phytoclasts, microcharcoal, smectite/illite,  
320 kaolinite/illite, abundance of chlorite and R1 I-S,  $Si/Al$ ,  $Zr/Rb$ ,  $Zr/Al$ ) were normalized between 0-1 and run for



- 321 PCA analysis in PAST. Sixty-four percent of the variance is explained by the first three axes (PCA-1 27.7 %,  
322 PCA-2 19.7 %, PCA-3 15.3 %) inside the 95 % confidence interval.
- 323 PC-1 mainly explains the anti-correlation of TOC and  $\text{CaCO}_3$ . PC-2 shows the anti-correlation of K/I and S/I.  
324 Positive loadings were observed for S/I, microcharcoal, macrocharcoal and  $\text{CaCO}_3$ . For PC-2, negative loadings  
325 were observed for K/I, abundance of chlorite + I-S R1. PC-3 shows strong positive loadings ( $> 0.3$ ) for  $\delta^{13}\text{C}_{\text{org}}$ ,  
326 Si/Al and Zr/Al.
- 327 Plotting PC-1 (y-axis) over PC-3 (x-axis) shows that the samples after the onset of the +ve CIE are grouped to  
328 the top of the y-axis (more associated with S/I compared to K/I) and to the right of the x-axis (more associated  
329 with primary minerals, phytoclasts, and higher Si/Al, Zr/Rb and Zr/Al) (Fig. 5).



- 330 **Figure 5: PCA-analysis shows a distinctly different depositional signature before and after the onset of**  
331 **the LPE +ve CIE in the Mochras core.** PCA plot of PC-1 and PC-3: all samples before the onset of the LPE  
332 +ve CIE are marked in black closed circles and the samples after the onset of the LPE +ve CIE are marked in  
333 blue open squares.

334

### 335 1.5 Discussion

- 336 Figure 2 provides the context for the LPE ‘cooling event’ at Mochras set within the background record. Shifts in  
337 bulk  $\delta^{18}\text{O}_{\text{carb}}$  are coeval to the  $\delta^{13}\text{C}_{\text{org}}$  change to heavier isotopic values (~930 mbs) and reach a maximum in the  
338 Margaritatus Zone ( $>1 \%$ ) (Ullmann *et al.*, 2022). The bulk oxygen-isotope excursions of Mochras are affected  
339 by diagenesis and are deemed unlikely to reflect environmental conditions (Ullmann *et al.*, 2022). However,



340 oxygen isotope data from marine benthic and nekto-benthic molluscs and brachiopods show heavier values  
341 during the late Margaritatus Zone concurrent with a positive shift in  $\delta^{13}\text{C}_{\text{org}}$ , indicating cooling during the LPE  
342 in the nearby Cleveland Basin (Robin Hood's Bay and Staithes) (Korte & Hesselbo, 2011) and this trend is also  
343 observed in several European sections (e.g. Korte *et al.*, 2015). The duration of the +ve CIE has been estimated  
344 as ~0.4–0.6 Myr in the Cardigan Bay Basin (Ruhl *et al.*, 2016; Storm *et al.*, 2020).

345

### 346 1.5.1 Background sedimentological and environmental variations

347 The Mochras succession shows metre-scale alternating TOC-enhanced and Ca-rich lithological couplets  
348 (mudstone/limestone; Fig. 2). Previous assessments of the palaeoenvironmental signature of these TOC-  
349 enhanced and Ca-rich couplets indicate strongly that the different depositional modes are driven by orbital  
350 precession (Ruhl *et al.*, 2016; Hinnov *et al.*, 2018; Storm *et al.*, 2020; Hollaar *et al.*, 2021; Pieńkowski *et al.*,  
351 2021). Precession driven changes in monsoonal strength have been suggested to influence the deposition and  
352 preservation of TOC and carbonate in the Cardigan Bay Basin (Ruhl *et al.*, 2016), although the impact may have  
353 been expressed, at least partially, by changes in strength of bottom currents in the seaway as a whole  
354 (Pieńkowski *et al.*, 2021).

355 The preservation of primary carbonate is poor in the Mochras borehole, making it complex to determine in  
356 detail the relative importance of carbonate producers for the bulk carbonate content (Ullmann *et al.*, 2022).  
357 However, Early Jurassic, pelagic settings in the Tethys region often received abiotic fine grained carbonate from  
358 shallow marine carbonate platforms (Weedon, 1986; Cobianchi & Picotti, 2001) and/or via carbonate producing  
359 organisms (such as coccolithophores in zooplankton pellets) (Weedon, 1986; van de Schootbrugge *et al.*, 2005,  
360 e.g. Weedon *et al.*, 2018). Coccolithophores are often poorly preserved and recrystallized (Weedon, 1986;  
361 Weedon *et al.*, 2018). The organic matter found in the studied section of the Mochras borehole varies between  
362 18 and 42% terrestrial phytoclasts (Fig. 3). Phytoclasts are common, but palynomorphs are relatively sparse and  
363 poorly preserved. Marine amorphous organic matter is the main constituent in the present study of particulate  
364 organic matter in unsieved macerated samples, in the interval studied here (951 – 918 mbs). Examination of  
365 variations in the terrestrial/marine proportions of organic matter, shows no correspondence between the type of  
366 organic matter and the TOC-enhanced or Ca-rich lithological alternations. However, previous research has  
367 indicated that the percentage of terrestrial phytoclasts show precession forcing independent of the lithological  
368 couplets (so out of phase with precession scale changes in Ca-TOC content) between 951 – 934 mbs in the  
369 Mochras core (Hollaar *et al.*, 2021). Such orbital forcing of the terrestrial vs marine proportions of organic  
370 matter were also found in Early Jurassic sediments of Dorset, and were similarly independent of the lithological  
371 facies (Waterhouse, 1999). Terrestrial phytoclast content show a weak expression of long-eccentricity driven  
372 variations in the section studied (Fig. 3).

373 Fossil charcoal makes up a substantial proportion of the organic fractions (11% of the terrestrial fraction) and  
374 has previously been shown to vary considerably over long-eccentricity cycle  $459 \pm 1$  peaking in abundance  
375 during the phase of maximum eccentricity (Hollaar *et al.*, 2021). Microcharcoal also appears to be most  
376 abundant during the maximum phase of the subsequent long eccentricity cycle  $458 \pm 1$  (Fig. 3). Additionally,  
377 K/I and S/I clay mineral ratios appear to alternate in response to long-eccentricity drivers (Fig. 3) up to 931 mbs



378 where the clay mineral signature changes. Between 951 and 930 mbs high K/I occurs during phases of low long  
379 eccentricity suggesting an enhanced hydrological cycle (Hollaar *et al.*, 2021) with more intense weathering, and  
380 enhanced fine grained terrestrial runoff to the marine record (Deconinck *et al.*, 2019). In contrast, phases of  
381 maximum long-eccentricity appear to be smectite-rich, indicating seasonal rainfall, enhanced fire (Hollaar *et al.*,  
382 2021) and thus periods of droughts, and lower terrestrial runoff and subsequent lower dilution (Deconinck *et al.*,  
383 2019). Detrital elemental ratios increase accordingly during the smectite-rich phases, and are lower during  
384 kaolinite-rich phases between 951 and 930 mbs. Detrital elemental ratios can be used to explore changes in  
385 sediment composition (e.g. Thibault *et al.*, 2018; Hesselbo *et al.*, 2020b) and the similarity of the long-term  
386 trend in Zr/Rb and Si/Al (Fig. 2) indicates that these elemental ratios reflect grainsize. The clay fraction (hosting  
387 Al, and Rb (Chen *et al.*, 1999)), diminishes upwards, whereas the coarser silt to sand fraction (associated with Si  
388 (Hesselbo *et al.*, 2020b) and Zr (Chen *et al.*, 2006)), increases upward (Fig. 3 and 4). The grainsize changes  
389 inferred here reflect two overall coarsening upwards sequences (Fig. 3 and 4). These sequences may reflect  
390 changes in clastic transport due to changes in the proximity to the shore/siliciclastic source, changes in runoff  
391 due to a changing hydrological cycle, or accelerated bottom currents with greater carrying capacity of coarser  
392 sediments.

393

#### 394 **1.5.2 Depositional and environmental changes before and after the LPE +ve CIE**

395 The LPE +ve CIE begins around 930 mbs in the Mochras core and encompasses the remaining part of the  
396 studied section (Fig. 3). We contrasted all the pre-CIE sediment signatures with those of the +ve CIE signatures  
397 using principal components analysis which indicates a distinctly different sedimentary composition and  
398 environmental signature before and after the onset of the +ve CIE in Mochras (Fig. 5).

399 Before the +ve CIE onset, the clay mineral assemblage shows alternating phases of smectite and kaolinite,  
400 indicating pedogenic weathering. The relative abundance of the detrital clay types observed in the studied  
401 interval have the potential to hold important palaeoclimatic information regarding the hydrological cycle and the  
402 relative proportion of chemical weathering and physical erosion. Chemical weathering is enhanced in a high  
403 humidity environment with relatively high temperatures and rainfall, when clays are formed in the first stages of  
404 soil development. In the modern day, kaolinite is primarily formed in tropical soils, under year-round rainfall  
405 and high temperatures (Thiry, 2000). Smectite also occurs in the tropics, but is more common in the subtropical  
406 to Mediterranean regions, where humidity is still high, but periods of drought also occur (Thiry, 2000). Hence,  
407 smectite forms predominantly in soil profiles under a warm and seasonally dry climate (Chamley, 1989; Raucsik  
408 & Varga, 2008), and kaolinite in a year-round humid climate (Chamley, 1989; Ruffell *et al.*, 2002). Similarly,  
409 alternating intervals of kaolinite and smectite dominance were observed for the Late Sinemurian (Munier *et al.*,  
410 2021) and the Pliensbachian of Mochras (Deconinck *et al.*, 2019). The predominantly detrital character of these  
411 clay minerals has been confirmed by TEM scanning of Pliensbachian smectite minerals, which revealed the  
412 fleecy morphology and lack of overgrowth (Deconinck *et al.*, 2019). Therefore, the alternations of smectite and  
413 kaolinite are interpreted to reflect palaeoclimatic signatures of a changing hydrological cycle, with a year-round  
414 wet climate evidenced by high K/I ratios, and a more monsoon-like climate with seasonal rainfall with high S/I  
415 (Deconinck *et al.*, 2019; Hollaar *et al.*, 2021; Munier *et al.*, 2021) (See Fig. 3). The intervals with a signal for



416 weaker seasons appears to correspond to phases of low eccentricity in the 405 kyr cycle, and signals of greater  
417 seasonality with periods of high more pronounced eccentricity (Fig. 3) in the 405 kyr cycle.

418 Higher frequency cycles are not observed in the clay mineral ratios, with no precession or obliquity forcing  
419 detected in the high-resolution part of the study 951 – 934 mbs (Hollaar *et al.*, 2021) and no expression of the  
420 100 kyr cycle in the record presented here. The formation of developed kaolinite-rich, and to a lesser extent  
421 smectite-rich soil profiles, requires a steady landscape for many tens of thousands of years, although the ~1 Myr  
422 timescale of Thiry (2000) seems excessive in our case given the clear expression of clay mineral changes  
423 through long-eccentricity cycles. Also, the transportation and deposition of continental clays will occur after soil  
424 formation and add further time between formation and final deposition (Chamley, 1989; Thiry, 2000). Thus,  
425 there is likely to be a lag of the climatic signal observed in the marine sediments (Chamley, 1989; Thiry, 2000).  
426 However, we note that high frequency climatic swings have been recorded in the clay mineral record in some  
427 instances, such as in the Lower Cretaceous in SE Spain (Moiroud *et al.*, 2012). The limestone-marl alternations  
428 there are enhanced in smectite versus kaolinite and illite, respectively, reflecting precession scale swings from a  
429 semi-arid to a tropical humid climate (Moiroud *et al.*, 2012). Precession and higher frequency shifts in the clay  
430 record are likely caused by fluctuations in runoff conditions rather than the formation of soils with a different  
431 clay fraction.

432 Directly after the initial +ve CIE shift from 930–924 mbs (Phase 1 of Fig. 3) little seems to change, and the  
433 system evidently continued to respond as before to the long eccentricity forcing, despite the predicted cooling  
434 (Korte & Hesselbo, 2011; Korte *et al.*, 2015; Gómez *et al.*, 2016). However, from around 924 mbs up to the top  
435 of the studied section (Phase 2 of Fig. 3) the clay mineral assemblage displays a distinctly different composition,  
436 with kaolinite dominating especially the early part of phase 2 of the LPE (Fig. 3). At the same time there is an  
437 enhancement of the primary minerals illite and chlorite, and I-S R1 (Fig. 3 and SI Fig. 1). Although an  
438 enhancement in detrital kaolinite indicates an acceleration of the hydrological cycle, detrital kaolinite is dual in  
439 origin and can also be derived from reworking of the primary source material (Deconinck *et al.*, 2019). If the  
440 climate is cooler, chemical weathering becomes less dominant and physical erosion of the bedrock becomes the  
441 main detrital source of clay minerals. In the Cardigan Bay Basin, the bedrock of the surrounding Variscan  
442 massifs (such as the Caledonian, Welsh and Irish massifs) were a likely source of these clays. In the Early  
443 Jurassic of the NW Tethys region, mica-illite and chlorite bearing Lower Paleozoic mudrock were emergent  
444 (Merriman, 2006; Deconinck *et al.*, 2019), hence the enhancement of illite and chlorite likely indicates physical  
445 erosion in the region surrounding the study site. Finally, authigenic clay particles could have been formed  
446 during burial diagenesis. At temperatures between 60–70 °C smectite illitization occurs and I-S R1 is formed;  
447 however, the high abundance of smectite in Mochras indicates limited burial diagenesis in the Mochras core  
448 (Deconinck *et al.*, 2019). Weak thermal diagenesis is confirmed for the Pliensbachian of Mochras, with  $T_{max}$   
449 between 421 °C and 434 °C (van de Schootbrugge *et al.*, 2005). Therefore, I-S R1 in Mochras is interpreted to  
450 be derived from chemical weathering of illite (Deconinck *et al.*, 2019). The coeval increase of these primary  
451 clay minerals, I-S R1 and kaolinite, indicate that during this period physical erosion dominated over soil  
452 chemical weathering (Deconinck *et al.*, 2019; Munier *et al.*, 2021). This is similar to what is observed for the  
453 latest Pliensbachian in Mochras (Deconinck *et al.*, 2019).



454 Erosion of weathering profiles transports clay minerals (including kaolinite and smectite) to the marine realm. In  
455 the ocean, the differential settling of kaolinite (near shore) and smectite (more distal) could occur based on the  
456 morphology and size of clay particles (Thiry, 2000). However, comparison of long-term inferred regional sea  
457 level changes from surrounding UK basins (Hesselbo, 2008) suggests that the relative proportions of smectite  
458 and kaolinite are not influenced by changes in relative sea level in the Pliensbachian of Mochras (Deconinck *et*  
459 *al.*, 2019). On the assumption that the coarsening upward sequences at Mochras are indicative of relative sea  
460 level change, it can also be argued that the proximity to shore did not impact the proportions of smectite and  
461 kaolinite with enhanced smectite during ‘proximal’ deposition and enhanced kaolinite at times of more ‘distal’  
462 deposition (Fig. 3).

463 We suggest that the first phase of the LPE (Fig. 3, phase 1) was characterised by repeated periods of rainfall in a  
464 seasonal climate forced by precession in which chemical weathering (smectite formation) dominated the  
465 sedimentary signatures. This corresponds to maximum long-eccentricity and shows the same climatic signature  
466 as during maximum eccentricity phases before the +ve CIE. This is then followed by a second phase (Fig. 3,  
467 phase 2) where the climate is generally cooler, overall potentially more arid, but with rainfall throughout the  
468 year over multiple precession cycles. This appears to have favoured deep physical erosion, owing to the  
469 abundance of primary clay minerals, kaolinite and I-S R1. This interval corresponds to a minimum phase in the  
470 405 kyr eccentricity based on Storm *et al.* (2020). This interpretation is further supported by decreasing and then  
471 low microcharcoal abundance, pointing to suppression of fire activity at this time.

472 Two coarsening upward cycles that predate the onset of the +ve CIE and continue for a few metres after its  
473 initiation, are present in the detrital elemental ratios (best expressed in Si/Al and Zr/Rb records) (Fig. 3 and 4),  
474 and indicate a changing sediment influx over the studied interval. Previous study of the lithofacies of the  
475 Mochras borehole has also shown the coarsening-upward sequences of 0.5–3 m thickness, which are observed to  
476 be followed upwards by a thinner fining-upward succession (Pieńkowski *et al.*, 2021). This reported fining-  
477 upward part is not reflected in the elemental ratios of the two sequences shown in this study. Furthermore, the  
478 coarsest phases of these sequences are approximately coeval with decreasing trends in the K/I ratio and  
479 increasing trends in the S/I. This could indicate that periods of a strong monsoonal/seasonal climate (indicated  
480 by S/I) brought coarser grained material to the basin, whereas periods of year-round humidity (K/I) are  
481 associated with higher chemical weathering (low Si/Al). Therefore, these two coarsening upwards cycles appear  
482 to link to increasing long-eccentricity. A similar mechanism has been inferred for the northern South China Sea  
483 region in the Miocene, where coarser grained material is found during periods of a strong summer monsoon and  
484 relatively lower chemical weathering (Clift *et al.*, 2014). Present day studies show that bedrock erosion and  
485 associated sediment transport is greater in areas with high seasonal contrast (Molnar, 2001; Molnar, 2004).  
486 Hence, the Si/Al record also appears to reflect weathering and erosion conditions on land (Clift *et al.*, 2014,  
487 2020), driven by long-eccentricity modulated climate (SI Fig.5). However, other scenarios that would influence  
488 the grain size on this time scale cannot be dismissed and include changes in proximity to siliciclastic source, or  
489 changes in sediment transport via bottom water currents.

490 Changes in bottom water current strength and direction likely affected the depositional site of the Mochras core  
491 (Pieńkowski *et al.*, 2021) although there is as yet no consensus on the processes that likely controlled these  
492 palaeoceanographic parameters. An early phase of regional tectonic updoming of the North Sea disrupted the



493 circulation in the N-S Laurasian Seaway (including the Viking Corridor) and therefore diminished the  
494 connectivity between western Tethys and the Boreal realm, hypothetically reducing poleward heat transport  
495 from the tropics (Korte *et al.*, 2015). This mechanism has also been argued to explain the later cooling observed  
496 in NW Europe during the transition of the warmer Toarcian to the cooler Aalenian and Bajocian (Korte *et al.*,  
497 2015). Late Pliensbachian occlusion of the Viking Corridor is supported by the provincialism of marine faunas  
498 at this time, showing a distinct Euro-Boreal province and a Mediterranean province (Dera *et al.*, 2011b). During  
499 the Toarcian a northward expansion of invertebrate faunal species has been found (Schweigert, 2005; Zakharov  
500 *et al.*, 2006; Bourillot *et al.*, 2008; Nikitenko, 2008), indicating a northward (warmer) flow through the Viking  
501 corridor (Korte *et al.*, 2015). More recently, a southward expansion of Arctic dinoflagellates into the Viking  
502 Corridor was suggested for the termination of the T-OAE (van de Schootbrugge *et al.*, 2019), which is in  
503 agreement with a N to S flow through the Viking Corridor suggested by numerical models (Bjerrum *et al.*, 2001;  
504 Dera & Donnadieu, 2012; Ruvalcaba Baroni *et al.* 2018) and sparse Nd-isotopes (Dera *et al.*, 2009).

505 Over the European Epicontinental Shelf (EES), and the Tethys as a whole, a clockwise circular gyre likely  
506 brought oxygenated warm Tethyan waters to the southwest shelf, with a progressively weaker north and  
507 eastward flow due to rough bathymetry and substantial islands palaeogeography (Ruvalcaba Baroni *et al.*,  
508 2018). This predominantly surface flow is modelled to have extended to shelfal sea floor depths. Only  
509 episodically might nutrient-rich Boreal waters have penetrated south onto the EES in these coupled ocean-  
510 atmosphere GCM model scenarios (Dera & Donnadieu, 2012). The modelling also suggests – counter-  
511 intuitively – that the clockwise surface gyre of the Tethys extended further northwards and impacted the EES  
512 more effectively when the Hispanic corridor was more open.

513 An alternative bottom current configuration was discussed for Mochras specifically wherein changes in north-  
514 to-south current strength (cf. Bjerrum *et al.*, 2001) are proposed for the changes in grainsize and siliciclastic  
515 versus clay content via contour currents (Pieńkowski *et al.*, 2021). A strong flow from the cooler and shallow  
516 boreal waters is hypothesized to have brought a coarser grainsize fraction in suspension and as bedload, which  
517 was then deposited in the Cardigan Bay Basin while flowing to the deeper and warmer waters of the peri-Tethys  
518 (Pieńkowski *et al.*, 2021). Times of a strong north to south current are proposed to be associated with more  
519 oxygenated bottom waters (Pieńkowski *et al.*, 2021). In contrast, when the north to south current became  
520 weaker, less coarse material will have been carried in suspension and as bedload, and a relatively higher clay  
521 proportion will have been deposited in the Cardigan Bay Basin (Pieńkowski *et al.*, 2021). In this scenario, times  
522 of sluggish currents are associated with low bottom water oxygenation (Pieńkowski *et al.*, 2021) and thus  
523 climate forcing of current strength could explain the deposition of alternating coarser and finer fractions in the  
524 Mochras borehole (Pieńkowski *et al.*, 2021).

525 Our research suggests that orbital cycles both before and during the onset of the +ve CIE have a significant  
526 influence on seasonality and hydrology, affecting both fire regimes and sediment depositional character. Further  
527 research is required to consider how long-eccentricity and obliquity cycles might interact with north-south flow  
528 in the Cardigan Bay Basin and circulation processes. What is clear is that orbital cycles have impact on  
529 terrestrial processes in the terrestrial sediment source areas (Hollaar *et al.*, 2021) and led to differences in  
530 deposition within the marine sediments in Mochras core (Ruhl *et al.*, 2016; Pieńkowski *et al.*, 2021). Our data  
531 indicate that periods of coarser sediment deposition correspond to periods that include more seasonal climates



532 before the onset of the +ve CIE (low kaolinite), which is in line with the hypothesized grainsize changes caused  
533 by contour currents (Pieńkowski *et al.*, 2021). However, after the onset of the +ve CIE, although we suggest that  
534 the chemical weathering rate decreased, enhanced runoff and physical erosion are indicated by a peak in primary  
535 clay minerals and K/I. Enhanced runoff could be expected to impact the thermohaline contour currents (Dera &  
536 Donnadieu, 2012). Simultaneously, an increasingly cold climate (as indicated by enhanced physical erosion over  
537 chemical weathering) indicates a boreal influence. It remains to be determined to what extent orbital cycles  
538 might have the power to influence ocean circulation in the basin.

539 Relatively coarse sediments in the Late Pliensbachian have also been related to shallower sediment deposition in  
540 UK basins (Hesselbo & Jenkyns, 1998; Hesselbo, 2008; Korte & Hesselbo, 2011). These regressive facies may  
541 have been caused by an early phase of North Sea doming (Korte & Hesselbo, 2011). Sequence stratigraphy of  
542 the Lower Jurassic of the Wessex, Cleveland and Hebrides basins (Hesselbo & Jenkyns, 1998; Hesselbo, 2008)  
543 shows relative sea level changes and sand influxes in the late Margaritatus Zone in the studied basins.  
544 Noteworthy in the Mochras borehole are phases of low  $\delta^{18}\text{O}$  of macrofossils which seem to correspond to high  
545 phases of macrofossil wood concomitant with low sea level, suggesting a possible control of relative sea level  
546 on the oxygen-isotope record and the source of detrital material (Ullmann *et al.*, 2022). The broad spatial  
547 distribution of these basins suggests that associated regression and/or sediment influx is of at least regional scale  
548 (Hesselbo, 2008). The results presented here fall within this phase of regression (Hesselbo & Jenkyns, 1998;  
549 Hesselbo, 2008).

550 In the context of North Sea doming as a possible cause of the Late Pliensbachian cooling, these facies can be  
551 interpreted to represent shallowing upward facies in a shallower system, or deep water system receiving coarser  
552 sediment input. The doming is hypothesized to have minimized or prohibited southward flow of cooler waters  
553 from the Boreal and northward flow from warmer waters from the Mediterranean area (Korte *et al.*, 2015). The  
554 Mochras borehole is situated on the southwestern flank of the dome and would have been cut-off from the  
555 northern parts of the Laurasian Seaway, including the Hebrides Basin and Cleveland Basin (Korte *et al.*, 2015).  
556 This change in seaway circulation could have impacted the source area of the detrital sediments in the Mochras  
557 borehole and brought the shallow shoreface facies closer to the borehole site.

558 Doming of the North Sea area would have led to greater radial spread of nearshore facies; however, owing to the  
559 strong eccentricity forcing that we interpret here, an additional factor that is influenced by the seasonal  
560 distribution of insolation forced by orbital cyclicity needs to be included. The Cardigan Bay Basin (Mochras) is  
561 positioned about 290 km to the SW of the Cleveland Basin and at a similar latitude, but to the W of the Wessex  
562 Basin (Ziegler, 1990; Torsvik & Cocks, 2017), and is therefore expected to be impacted by the regional changes  
563 in sea level and/or sediment flux. In the Late Pliensbachian of the Cleveland Basin, the detrital ratios of Si/Al,  
564 Zr/Al and Zr/Rb show similar coarsening upward sequences, which have been interpreted to reflect changes in  
565 riverine transport of siliciclastic grains and grainsize (Thibault *et al.*, 2018). The inferred changes in sea-level in  
566 the Cleveland Basin occur at a 100 kyr pacing (Huang & Hesselbo, 2014; Hesselbo *et al.*, 2020b), potentially  
567 linking the regression cycles to short eccentricity (Huang *et al.*, 2010 and refs therein) and long-eccentricity  
568 (Thibault *et al.*, 2018). This would mean that eccentricity driven changes in inferred sea level change could be  
569 linked to glacioeustatic cycles during these times (Brandt, 1986; Suan *et al.*, 2010; Korte & Hesselbo, 2011;  
570 Krencker *et al.*, 2019; Ruebsam *et al.*, 2019, 2020b; Ruebsam & Schwark, 2021; Ruebsam & Al-Husseini,



571 2021). Glacioeustatic sea level changes are discussed for the Early Jurassic and Middle Jurassic (Krencker *et al.*,  
572 2019; Bodin *et al.*, 2020; Ruebsam & Schwark, 2021; Nordt *et al.*, 2022). A recent study on the rapid  
573 transgression observed at the Pliensbachian–Toarcian boundary, ruled out other mechanisms that could force sea  
574 level at this time scale, such as aquifer-eustacy, and show that glacioeustatic changes in sea level are a likely  
575 possibility at times in the Early Jurassic (Krencker *et al.*, 2019). Therefore, our findings overall provide support  
576 the episodic occurrence of continental ice at the poles (Brandt, 1986; Price, 1999; Suan *et al.*, 2010; Korte &  
577 Hesselbo, 2011; Korte *et al.*, 2015; Bougeault *et al.*, 2017; Krencker *et al.*, 2019; Ruebsam *et al.*, 2019, 2020a,  
578 2020b; Ruebsam & Schwark, 2021; Ruebsam & Al-Husseini, 2021).

579

## 580 1.6 Conclusions

581 The terrestrial environment adjacent to the Cardigan Bay Basin was strongly influenced by both orbitally driven  
582 climate forcings and the Late Pliensbachian Cooling Event (LPE). Long-eccentricity forcing remained strong  
583 both prior to and during the LPE. Prior to the LPE, eccentricity-driven shifts in maximum seasonality influence  
584 the degree of chemical weathering (S/I vs K/I), sediment flux to the basin (Si/Al), and fire activity. As maximum  
585 precessional seasonality decreases with reduced 405 kyr eccentricity, the year-round relatively cool and wet  
586 climate extended over multiple precession cycles drove significant erosion of bedrock on emergent land surfaces  
587 as evidenced by high bedrock-derived mineral content, high K/I and I-S R1. Therefore, both the Milankovitch  
588 forcings and larger climatic shifts operate in tandem to drive changes in the terrestrial environment.

589

590 **Data availability:** Supplementary data is available at the National Geoscience Data Centre at Keyworth  
591 (NGDC) at (doi to be added) for the interval 934 – 918 mbs. All data presented for the interval 951 – 934 mbs is  
592 available at the National Geoscience Data Centre at Keyworth (NGDC) at [https://doi.org/10.5285/d6b7c567-](https://doi.org/10.5285/d6b7c567-49f0-44c7-a94c-e82fa17ff98e)  
593 [49f0-44c7-a94c-e82fa17ff98e](https://doi.org/10.5285/d6b7c567-49f0-44c7-a94c-e82fa17ff98e) (Hollaar *et al.*, 2021). The full Mochras XRF dataset is in Damaschke *et al.*  
594 (2021).

595 **Author contribution:** CMB, SPH and TPH designed the research. TPH conducted the laboratory  
596 measurements, with JFD contributing to the XRD-measurements and MD, CU and ML to the XRF-  
597 measurements. TPH, CMB and SPH wrote the manuscript, with contributions of all authors.

598 **Competing interests:** The authors declare that they have no conflict of interest.

599 **Acknowledgements:** This is a contribution to the JET project funded by the Natural Environment Research  
600 Council (NERC) (grant number NE/N018508/1). SPH, CMB, JFD, CU, ML and TPH, acknowledge funding  
601 from the International Continental Scientific Drilling Program (ICDP) and TPH acknowledges funding from the  
602 University of Exeter. We thank the British Geological Survey (BGS), especially James Riding, Scott Renshaw  
603 for facilitating access to the Mochras core. Also, Simon Wylde and Charles Gowing for their contribution to the  
604 XRF scanning and discussion on the results. We further thank Chris Mitchell for help with the TOC and  $\delta^{13}\text{C}_{\text{org}}$   
605 analyses. Finally, we thank Ludovic Bruneau for technical assistance with the XRD-analysis.

606



607 **References**

- 608 Alberti, M., Fürsich, F. T., and Andersen, N.: First steps in reconstructing Early Jurassic sea water temperatures  
609 in the Andean Basin of northern Chile based on stable isotope analyses of oyster and brachiopod shells, *J.*  
610 *Palaeogeogr.*, 8(1), 1 – 17, <https://doi.org/10.1186/s42501-019-0048-0>, 2019.
- 611 Alberti, M., Parent, H., Garrido, A. C., Andersen, N., Garbe-Schönberg, D., and Danise, S.: Stable isotopes  
612 ( $\delta^{13}\text{C}$ ,  $\delta^{18}\text{O}$ ) and element ratios (Mg/Ca, Sr/Ca) of Jurassic belemnites, bivalves and brachiopods from the  
613 Neuquén Basin (Argentina): challenges and opportunities for palaeoenvironmental reconstructions, *J. Geol.*  
614 *Soc.*, 178(1), <https://doi.org/10.1144/jgs2020-16>, 2021.
- 615 Bailey, T. R., Rosenthal, Y., McArthur, J. M., Van de Schootbrugge, B., and Thirlwall, M. F.:  
616 Paleooceanographic changes of the Late Pliensbachian–Early Toarcian interval: a possible link to the genesis of  
617 an Oceanic Anoxic Event, *Earth Planet. Sc. Lett.*, 212(3 – 4), 307 – 320, [https://doi.org/10.1016/S0012-](https://doi.org/10.1016/S0012-821X(03)00278-4)  
618 [821X\(03\)00278-4](https://doi.org/10.1016/S0012-821X(03)00278-4), 2003.
- 619 Beckmann, B., Flögel, S., Hofmann, P., Schulz, M., and Wagner, T.: Upper Cretaceous African climate  
620 development and implications for the marine carbon cycle, *Nature*, 437, 241 – 244,  
621 <https://doi.org/10.1038/nature03976>, 2005.
- 622 Belcher, C. M., Collinson, M. E., and Scott, A. C.: Constraints on the thermal energy released from the  
623 Chicxulub impactor: new evidence from multi-method charcoal analysis, *J. Geol. Soc.*, 162(4), 591 – 602,  
624 <https://doi.org/10.1144/0016-764904-104>, 2005.
- 625 Bjerrum, C. J., Surlyk, F., Callomon, J. H., and Slingerland, R. L.: Numerical paleooceanographic study of the  
626 Early Jurassic transcontinental Lurasian Seaway, *Paleoceanography*, 16(4), 390 – 404,  
627 <https://doi.org/10.1029/2000PA000512>, 2001.
- 628 Bodin, S., Mau, M., Sadki, D., Danisch, J., Nutz, A., Krencker, F. N., and Kabiri, L.: Transient and secular  
629 changes in global carbon cycling during the early Bajocian event: Evidence for Jurassic cool climate episodes,  
630 *Global Planet. Change*, 194, 103287, <https://doi.org/10.1016/j.gloplacha.2020.103287>, 2020.
- 631 Bougeault, C., Pellenard, P., Deconinck, J.F., Hesselbo, S.P., Dommergues, J.L., Bruneau, L., Cocquerez, T.,  
632 Laffont, R., Huret, E. and Thibault, N.: Climatic and palaeoceanographic changes during the Pliensbachian  
633 (Early Jurassic) inferred from clay mineralogy and stable isotope (CO) geochemistry (NW Europe), *Global*  
634 *Planet. Change*, 149, <https://doi.org/10.1016/j.gloplacha.2017.01.005>, 2017.
- 635 Bourillot, R., Neige, P., Pierre, A., and Durlot, C.: Early–middle Jurassic Lytoceratid ammonites with  
636 constrictions from Morocco: palaeobiogeographical and evolutionary implications, *Palaeontology*, 51(3), 597 –  
637 609, <https://doi.org/10.1111/j.1475-4983.2008.00766.x>, 2008.
- 638 Brandt, K.: Glacioeustatic cycles in the Early Jurassic?, *Neues Jahrbuch für Geologie und Paläontologie-*  
639 *Monatshefte*, 257 – 274, <https://doi.org/10.1127/njgpm/1986/1986/257>, 1986.



- 640 Calvert, S. E., and Pedersen, T. F.: Chapter fourteen elemental proxies for palaeoclimatic and  
641 palaeoceanographic variability in marine sediments: interpretation and application, *Dev. Mar. Geol.*, 1, 567 –  
642 644, [https://doi.org/10.1016/S1572-5480\(07\)01019-6](https://doi.org/10.1016/S1572-5480(07)01019-6), 2007.
- 643 Chamley, H.: *Clay Sedimentology*, Springer Verlag, Berlin, 623 pp., ISBN 978-3-642-85918-8, 1989.
- 644 Chen, J., An, Z., and Head, J.: Variation of Rb/Sr ratios in the loess-paleosol sequences of central China during  
645 the last 130,000 years and their implications for monsoon paleoclimatology, *Quat. Res.*, 51(3), 215 – 219,  
646 <https://doi.org/10.1006/qres.1999.2038>, 1999.
- 647 Chen, J., Chen, Y., Liu, L., Ji, J., Balsam, W., Sun, Y., and Lu, H.: Zr/Rb ratio in the Chinese loess sequences  
648 and its implication for changes in the East Asian winter monsoon strength, *Geochim. Cosmochim. Acta*, 70(6),  
649 1471 – 1482, <https://doi.org/10.1016/j.gca.2005.11.029>, 2006.
- 650 Cifer, T., Goričan, Š., Auer, M., Demény, A., Fraguas, Á., Gawlick, H. J., and Riechelmann, S.: Integrated  
651 stratigraphy (radiolarians, calcareous nannofossils, carbon and strontium isotopes) of the Sinemurian–  
652 Pliensbachian transition at Mt. Rettenstein, Northern Calcareous Alps, Austria, *Global Planet. Change*, 212,  
653 103811, <https://doi.org/10.1016/j.gloplacha.2022.103811>, 2022.
- 654 Clift, P. D., Kulhanek, D. K., Zhou, P., Bowen, M. G., Vincent, S. M., Lyle, M., and Hahn, A.: Chemical  
655 weathering and erosion responses to changing monsoon climate in the Late Miocene of Southwest Asia, *Geol.*  
656 *Mag.*, 157(6), 939 – 955, <https://doi.org/10.1017/S0016756819000608>, 2020.
- 657 Clift, P. D., Wan, S., and Blusztajn, J.: Reconstructing chemical weathering, physical erosion and monsoon  
658 intensity since 25 Ma in the northern South China Sea: a review of competing proxies, *Earth Sci. Rev.*, 130, 86  
659 – 102, <https://doi.org/10.1016/j.earscirev.2014.01.002>, 2014.
- 660 Copestake, P., and Johnson, B.: Lower Jurassic Foraminifera from the Llanbedr (Mochras Farm) Borehole,  
661 North Wales, UK, *Monographs of the Palaeontographical Society*, 167(641), 1 – 403, 2014.
- 662 Damaschke, M., Wylde, S., Jiang, M., Hollaar, T., Ullmann, C.V.: Llanbedr (Mochras Farm) Core Scanning  
663 Dataset. NERC EDS National Geoscience Data Centre. (Dataset). [https://doi.org/10.5285/c09e9908-6a21-43a8-  
664 bc5a-944f9eb8b97e](https://doi.org/10.5285/c09e9908-6a21-43a8-bc5a-944f9eb8b97e), 2021.
- 665 Damborenea, S. E., Echevarria, J., and Ros-Franch, S.: Southern Hemisphere Palaeobiogeography of Triassic–  
666 Jurassic Marine Bivalves, *Springer Briefs Seaways and Landbridges: Southern Hemisphere Biogeographic  
667 Connections Through Time*, Springer Science & Business Media, Berlin, [https://doi.org/10.1007/978-94-007-  
5098-2\\_1](https://doi.org/10.1007/978-94-007-<br/>668 5098-2_1), 2013.
- 669 Daniau, A. L., Sánchez Goñi, M. F., Martinez, P., Urrego, D. H., Bout-Roumazeilles, V., Desprat, S., and  
670 Marlon, J. R.: Orbital-scale climate forcing of grassland burning in southern Africa, *Proceedings of the National  
671 Academy of Sciences*, 110(13), 5069–5073, <https://doi.org/10.1073/pnas.1214292110>, 2013.
- 672 Deconinck, J. F., Hesselbo, S. P., and Pellenard, P.: Climatic and sea-level control of Jurassic (Pliensbachian)  
673 clay mineral sedimentation in the Cardigan Bay Basin, Llanbedr (Mochras Farm) borehole, Wales,  
674 *Sedimentology*, 66, 2769–2783, <https://doi.org/10.1111/sed.12610>, 2019.



- 675 Dera, G., and Donnadieu, Y.: Modeling evidences for global warming, Arctic seawater freshening, and sluggish  
676 oceanic circulation during the Early Toarcian anoxic event, *Paleoceanography*, 27(2),  
677 <https://doi.org/10.1029/2012PA002283>, 2012.
- 678 Dera, G., Neige, P., Dommergues, J. L., and Brayard, A.: Ammonite paleobiogeography during the  
679 Pliensbachian–Toarcian crisis (Early Jurassic) reflecting paleoclimate, eustasy, and extinctions, *Global Planet.*  
680 *Change*, 78(3 – 4), 92 – 105, <https://doi.org/10.1016/j.gloplacha.2011.05.009>, 2011.
- 681 Dera, G., Pucéat, E., Pellenard, P., Neige, P., Delsate, D., Joachimski, M. M., Reisberg, L., and Martinez, M.:  
682 Water mass exchange and variations in seawater temperature in the NW Tethys during the Early Jurassic:  
683 evidence from neodymium and oxygen isotopes of fish teeth and belemnites, *Earth Planet. Sc. Lett.*, 286, 198–  
684 207, <https://doi.org/10.1016/j.epsl.2009.06.027>, 2009.
- 685 de Graciansky, P. C., Jacquin, T., and Hesselbo, S.P. (Eds.): The Ligurian cycle: An overview of Lower Jurassic  
686 2nd-order transgressive-regressive facies cycles in western Europe, *Mesozoic and Cenozoic Sequence*  
687 *Stratigraphy of European Basins*, SEPM special publication, 60, 467 – 479, ISBN 1-565776-043-3, 1998.
- 688 De Lena, L.F., Taylor, D., Guex, J., Bartolini, A., Adatte, T., van Acken, D., Spangenberg, J.E., Samankassou,  
689 E., Vennemann, T. and Schaltegger, U.: The driving mechanisms of the carbon cycle perturbations in the late  
690 Pliensbachian (Early Jurassic), *Sci. Rep-UK*, 9(1), 1 – 12, <https://doi.org/10.1038/s41598-019-54593-1>, 2019.
- 691 Dobson, M. R. and Whittington, R. J.: The geology of Cardigan Bay, *P. Geologist. Assoc.*, 98, 331–353,  
692 [https://doi.org/10.1016/S0016-7878\(87\)80074-3](https://doi.org/10.1016/S0016-7878(87)80074-3), 1987.
- 693 Franceschi, M., Dal Corso, J., Posenato, R., Roghi, G., Masetti, D., and Jenkyns, H. C.: Early Pliensbachian  
694 (Early Jurassic) C-isotope perturbation and the diffusion of the Lithiotis Fauna: insights from the western  
695 Tethys, *Palaeogeogr. Palaeocl.*, 410, 255 – 263, <https://doi.org/10.1016/j.palaeo.2014.05.025>, 2014.
- 696 Gómez, J. J., Comas-Rengifo, M. J., and Goy, A.: Palaeoclimatic oscillations in the Pliensbachian (Early  
697 Jurassic) of the Asturian Basin (Northern Spain), *Clim. Past*, 12(5), 1199 – 1214, <https://doi.org/10.5194/cp-12-1199-2016>, 2016.
- 699 Hallam, A.: A revised sea-level curve for the early Jurassic, *J. Geol. Soc.*, 138(6), 735 – 743,  
700 <https://doi.org/10.1144/gsjgs.138.6.0735>, 1981.
- 701 Hesselbo, S. P., Bjerrum, C. J., Hinnov, L. A., MacNiocail, C., Miller, K. G., Riding, J. B., van de  
702 Schootbrugge, B., and the Mochras Revisited Science Team: Mochras borehole revisited: a new global standard  
703 for Early Jurassic earth history, *Sci. Dril.*, 16, 81–91, <https://doi.org/10.5194/sd-16-81-2013>, 2013.
- 704 Hesselbo, S. P., and Jenkyns, H. C. (Eds.): British Lower Jurassic sequence stratigraphy, *Mesozoic and*  
705 *Cenozoic Sequence Stratigraphy of European Basins*, SEPM special publication, 60, 561 – 581, ISBN 1-  
706 565776-043-3, 1998.
- 707 Hesselbo, S. P.: Sequence stratigraphy and inferred relative sea-level change from the onshore British Jurassic,  
708 *P. Geologist. Assoc.*, 119, 19–34, [https://doi.org/10.1016/S0016-7878\(59\)80069-9](https://doi.org/10.1016/S0016-7878(59)80069-9), 2008.



- 709 Hesselbo, S. P., Ogg, J. G., Ruhl, M., Hinnov, L. A., and Huang, C. J.: The Jurassic Period, in: Geological Time  
710 Scale 2020, edited by: Gradstein, F. M., Ogg, J. G., Schmitz, M. D., and Ogg, G. M. (Eds.), Elsevier, 955 –  
711 1021, 2020a.
- 712 Hesselbo, S. P., Hudson, A. J. L., Huggett, J. M., Leng, M. J., Riding, J. B., and Ullmann, C. V.: Palynological,  
713 geochemical, and mineralogical characteristics of the Early Jurassic Liasidium Event in the Cleveland Basin,  
714 Yorkshire, UK, *Newsl. Stratigr.*, 53, 191–211, <https://doi.org/10.1127/nos/2019/0536>, 2020b.
- 715 Hinnov, L.A., Ruhl, M., and Hesselbo, S.P.: Reply to the Comment on “Astronomical constraints on the  
716 duration of the Early Jurassic Pliensbachian Stage and global climatic fluctuations” [*Earth Planet. Sci. Lett.* 455  
717 (2016) 149 – 165], *Earth Planet. Sc. Lett.*, 481, 415 – 419, <https://doi.org/10.1016/j.epsl.2016.08.038>, 2018.
- 718 Hollaar, T. P., Baker, S. J., Hesselbo, S. P., Deconinck, J. F., Mander, L., Ruhl, M., and Belcher, C. M.:  
719 Wildfire activity enhanced during phases of maximum orbital eccentricity and precessional forcing in the Early  
720 Jurassic, *Commun. Earth Environ.*, 2(1), 1 – 12, <https://doi.org/10.1038/s43247-021-00307-3>, 2021.
- 721 Huang, C., and Hesselbo, S. P.: Pacing of the Toarcian Oceanic Anoxic Event (Early Jurassic) from  
722 astronomical correlation of marine sections, *Gondwana Res.*, 25(4), 1348 – 1356,  
723 <https://doi.org/10.1016/j.gr.2013.06.023>, 2014.
- 724 Huang, C., Hesselbo, S. P., and Hinnov, L.: Astrochronology of the late Jurassic Kimmeridge Clay (Dorset,  
725 England) and implications for Earth system processes, *Earth Planet. Sc. Lett.*, 289(1 – 2), 242 – 255,  
726 <https://doi.org/10.1016/j.epsl.2009.11.013>, 2010.
- 727 Ilyina, V. I.: Jurassic palynology of Siberia, Hayka, 1985.
- 728 Ivimey-Cook, H. C.: Stratigraphical palaeontology of the Lower Jurassic of the Llanbedr (Mochras Farm)  
729 Borehole, in: *The Llandbedr (Mochras Farm) Borehole*, edited by: Woodland, A. W., 87 – 92, (Rep. No. 71/18,  
730 Institute of Geological Sciences, 1971), 1971.
- 731 Jenkyns, H. C., and Clayton, C. J.: Black shales and carbon isotopes in pelagic sediments from the Tethyan  
732 Lower Jurassic, *Sedimentology*, 33(1), 87 – 106, <https://doi.org/10.1111/j.1365-3091.1986.tb00746.x>, 1986.
- 733 Kaplan, M. E.: Calcite pseudomorphoses in Jurassic and Lower Cretaceous deposits of the northern area of  
734 eastern Siberia, *Geologiya i Geofizika*, 19, 62 – 70, 1978.
- 735 Korte, C., Hesselbo, S. P., Ullmann, C. V., Dietl, G., Ruhl, M., Schweigert, G., and Thibault, N.: Jurassic  
736 climate mode governed by ocean gateway, *Nat Commun*, 6(1), 1 – 7, <https://doi.org/10.1038/ncomms10015>, 2015.
- 737 Korte, C. and Hesselbo, S. P.: Shallow-marine carbon- and oxygen-isotope and elemental records indicate  
738 icehouse-greenhouse cycles during the Early Jurassic, *Paleoceanography*, 26, PA4219,  
739 <https://doi.org/10.1029/2011PA002160>, 2011.
- 740 Krencker, F. N., Lindström, S., and Bodin, S.: A major sea-level drop briefly precedes the Toarcian oceanic  
741 anoxic event: implication for Early Jurassic climate and carbon cycle, *Sci Rep-UK*, 9(1), 1 – 12,  
742 <https://doi.org/10.1038/s41598-019-48956-x>, 2019.



- 743 Laskar, J., Fienga, A., Gastineau, M., and Manche, H.: La2010: a new orbital solution for the long-term motion  
744 of the Earth, *Astron Astrophys*, 532, A89, <https://doi.org/10.1051/0004-6361/201116836>, 2011.
- 745 McArthur, J. M., Donovan, D. T., Thirlwall, M. F., Fouke, B. W., and Matthey, D.: Strontium isotope profile of  
746 the early Toarcian (Jurassic) oceanic anoxic event, the duration of ammonite biozones, and belemnite  
747 palaeotemperatures, *Earth Planet. Sc. Lett.*, 179(2), 269 – 285, [https://doi.org/10.1016/S0012-821X\(00\)00111-4](https://doi.org/10.1016/S0012-821X(00)00111-4),  
748 2000.
- 749 McElwain, J. C., Wade-Murphy, J., and Hesselbo, S. P.: Changes in carbon dioxide during an oceanic anoxic  
750 event linked to intrusion into Gondwana coals, *Nature*, 435(7041), 479 – 482,  
751 <https://doi.org/10.1038/nature03618>, 2005.
- 752 Mercuzot, M., Pellenard, P., Durllet, C., Bougeault, C., Meister, C., Dommergues, J. L., ... and El Hmidi, K.:  
753 Carbon-isotope events during the Pliensbachian (Lower Jurassic) on the African and European margins of the  
754 NW Tethyan Realm, *Newsl. Stratigr.*, 41 – 69, <https://doi.org/10.1127/nos/2019/0502>, 2020.
- 755 Merriman, R. J.: Clay mineral assemblages in British Lower Palaeozoic mudrocks, *Clay Miner.*, 41, 473–512,  
756 <https://doi.org/10.1180/0009855064110204>, 2006.
- 757 Moiroud, M., Martinez, M., Deconinck, J. F., Monna, F., Pellenard, P., Riquier, L., and Company, M.: High-  
758 resolution clay mineralogy as a proxy for orbital tuning: example of the Hauterivian–Barremian transition in the  
759 Betic Cordillera (SE Spain), *Sediment. Geol.*, 282, 336 – 346, <https://doi.org/10.1016/j.sedgeo.2012.10.004>,  
760 2012.
- 761 Molnar, P.: Climate change, flooding in arid environments, and erosion rates, *Geology*, 29(12), 1071 – 1074,  
762 [https://doi.org/10.1130/0091-7613\(2001\)029<1071:CCFIAE>2.0.CO;2](https://doi.org/10.1130/0091-7613(2001)029<1071:CCFIAE>2.0.CO;2), 2001.
- 763 Molnar, P.: Late Cenozoic increase in accumulation rates of terrestrial sediment: How might climate change  
764 have affected erosion rates?, *Annu. Rev. Earth Pl. Sc.*, 32, 67 – 89,  
765 <https://doi.org/10.1146/annurev.earth.32.091003.143456>, 2004.
- 766 Moore, D. M. and Reynolds, R. C.: *X-Ray Diffraction and the Identification and Analysis of Clay Minerals*,  
767 Oxford University Press, New York, 378 pp., ISBN 0 19 508713 5, 1997.
- 768 Morettini, E., Santantonio, M., Bartolini, A., Cecca, F., Baumgartner, P. O., and Hunziker, J. C.: Carbon isotope  
769 stratigraphy and carbonate production during the Early–Middle Jurassic: examples from the Umbria–Marche–  
770 Sabina Apennines (central Italy), *Palaeogeogr. Palaeoclimatol.*, 184(3 – 4), 251 – 273, [https://doi.org/10.1016/S0031-0182\(02\)00258-4](https://doi.org/10.1016/S0031-0182(02)00258-4), 2002.
- 772 Munier, T., Deconinck, J.F., Pellenard, P., Hesselbo, S.P., Riding, J.B., Ullmann, C.V., Bougeault, C.,  
773 Mercuzot, M., Santoni, A.L., Huret, É. and Landrein, P.: Million-year-scale alternation of warm–humid and  
774 semi-arid periods as a mid-latitude climate mode in the Early Jurassic (late Sinemurian, Laurasian  
775 Seaway), *Clim. Past*, 17(4), 1547 – 1566, <https://doi.org/10.5194/cp-17-1547-2021>, 2021.



- 776 Nikitenko, B. L.: The Early Jurassic to Aalenian paleobiogeography of the Arctic Realm: implication of  
777 microbenthos (Foraminifers and Ostracodes), *Stratigr. Geol. Correl.*, 16(1), 59 – 80,  
778 <https://doi.org/10.1007/s11506-008-1005-z>, 2008.
- 779 Nordt, L., Breecker, D., and White, J.: Jurassic greenhouse ice-sheet fluctuations sensitive to atmospheric CO<sub>2</sub>  
780 dynamics, *Nat. Geosci.*, 15(1), 54 – 59, <https://doi.org/10.1038/s41561-021-00858-2>, 2022.
- 781 Oboh-Ikuenobe, F. E., Obi, C. G., and Jaramillo, C. A.: Lithofacies, palynofacies, and sequence stratigraphy of  
782 Palaeogene strata in Southeastern Nigeria, *J. Afr. Earth Sci.*, 41(1 – 2), 79 – 101,  
783 <https://doi.org/10.1016/j.jafrearsci.2005.02.002>, 2005.
- 784 Petschick, R.: MacDiff 4.2.2, available at: <http://servermac.geologie.unfrankfurt.de/Rainer.html>, 2000.
- 785 Pieńkowski, G., Uchman, A., Ninard, K., and Hesselbo, S. P.: Ichnology, sedimentology, and orbital cycles in  
786 the hemipelagic Early Jurassic Laurasian Seaway (Pliensbachian, Cardigan Bay Basin, UK), *Global Planet.*  
787 *Change*, 207, 103648, <https://doi.org/10.1016/j.gloplacha.2021.103648>, 2021.
- 788 Price, G. D.: The evidence and implications of polar ice during the Mesozoic, *Earth Sci. Rev.*, 48(3), 183 – 210,  
789 [https://doi.org/10.1016/S0012-8252\(99\)00048-3](https://doi.org/10.1016/S0012-8252(99)00048-3), 1999.
- 790 Price, G. D., Baker, S. J., Van De Velde, J., and Clémence, M. E.: High-resolution carbon cycle and seawater  
791 temperature evolution during the Early Jurassic (Sinemurian–Early Pliensbachian), *Geochem. Geophys. Geosy.*,  
792 17(10), 3917 – 3928, <https://doi.org/10.1002/2016GC006541>, 2016.
- 793 Quesada, S., Robles, S., and Rosales, I.: Depositional architecture and transgressive–regressive cycles within  
794 Liassic backstepping carbonate ramps in the Basque–Cantabrian Basin, northern Spain, *J. Geol. Soc.*, 162(3),  
795 531 – 548, <https://doi.org/10.1144/0016-764903-041>, 2005.
- 796 Raucsik, B., and Varga, A.: Climato-environmental controls on clay mineralogy of the Hettangian–Bajocian  
797 successions of the Mecsek Mountains, Hungary: an evidence for extreme continental weathering during the  
798 early Toarcian oceanic anoxic event, *Palaeogeogr. Palaeoclimatol.*, 265(1 – 2), 1 – 13,  
799 <https://doi.org/10.1016/j.palaeo.2008.02.004>, 2008.
- 800 Riding, J. B., Leng, M. J., Kender, S., Hesselbo, S. P., and Feist-Burkhardt, S.: Isotopic and palynological  
801 evidence for a new Early Jurassic environmental perturbation, *Palaeogeogr. Palaeoclimatol.*, 374, 16 – 27,  
802 <https://doi.org/10.1016/j.palaeo.2012.10.019>, 2013.
- 803 Rogov, M. A., and Zakharov, V. A.: Jurassic and Lower Cretaceous glendonite occurrences and their  
804 implication for Arctic paleoclimate reconstructions and stratigraphy, *Earth Science Frontiers*, 17(Special Issue),  
805 345 – 347, 2010.
- 806 Rosales, I., Quesada, S., and Robles, S.: Paleotemperature variations of Early Jurassic seawater recorded in  
807 geochemical trends of belemnites from the Basque–Cantabrian basin, northern Spain, *Palaeogeogr.*  
808 *Palaeoclimatol.*, 203(3 – 4), 253 – 275, [https://doi.org/10.1016/S0031-0182\(03\)00686-2](https://doi.org/10.1016/S0031-0182(03)00686-2), 2004.



- 809 Rosales, I., Quesada, S., and Robles, S.: Geochemical arguments for identifying second-order sea-level changes  
810 in hemipelagic carbonate ramp deposits, *Terra Nova*, 18(4), 233 – 240, [https://doi.org/10.1111/j.1365-](https://doi.org/10.1111/j.1365-3121.2006.00684.x)  
811 [3121.2006.00684.x](https://doi.org/10.1111/j.1365-3121.2006.00684.x), 2006.
- 812 Ruebsam, W., and Al-Husseini, M.: Orbitally synchronized late Pliensbachian–early Toarcian glacio-eustatic  
813 and carbon-isotope cycles, *Palaeogeogr. Palaeoclimatol.*, 577, 110562, <https://doi.org/10.1016/j.palaeo.2021.110562>,  
814 2021.
- 815 Ruebsam, W., Mayer, B., and Schwark, L.: Cryosphere carbon dynamics control early Toarcian global warming  
816 and sea level evolution, *Global Planet. Change*, 172, 440 – 453, <https://doi.org/10.1016/j.gloplacha.2018.11.003>,  
817 2019.
- 818 Ruebsam, W., and Schwark, L.: Impact of a northern-hemispherical cryosphere on late Pliensbachian–early  
819 Toarcian climate and environment evolution, *Geol. Soc. Spec. Publ. London*, 514(1), 359 – 385,  
820 <https://doi.org/10.1144/SP514-2021-1>, 2021.
- 821 Ruebsam, W., Reolid, M., Sabatino, N., Masetti, D., and Schwark, L.: Molecular paleothermometry of the early  
822 Toarcian climate perturbation, *Global Planet. Change*, 195, 103351,  
823 <https://doi.org/10.1016/j.gloplacha.2020.103351>, 2020a.
- 824 Ruebsam, W., Thibault, N., and Al-Husseini, M.: Early Toarcian glacio-eustatic unconformities and  
825 chemostratigraphic black holes, in: *Stratigraphy and Timescales*, edited by: Montenari, M., 629 – 676,  
826 Academic Press, <https://doi.org/10.1016/bs.sats.2020.08.006>, 2020b.
- 827 Ruffell, A., McKinley, J. M., and Worden, R. H.: Comparison of clay mineral stratigraphy to other proxy  
828 palaeoclimate indicators in the Mesozoic of NW Europe, *Philos. T. Roy. Soc. A*, 360(1793), 675 – 693,  
829 <https://doi.org/10.1098/rsta.2001.0961>, 2002.
- 830 Ruhl, M., Hesselbo, S. P., Hinnov, L., Jenkyns, H. C., Xu, W., Riding, J. B., ... and Leng, M. J.: Astronomical  
831 constraints on the duration of the Early Jurassic Pliensbachian Stage and global climatic fluctuations, *Earth*  
832 *Planet. Sc. Lett.*, 455, 149 – 165, <https://doi.org/10.1016/j.epsl.2016.08.038>, 2016.
- 833 Ruvalcaba Baroni, I., Pohl, A., van Helmond, N. A., Papadomanolaki, N. M., Coe, A. L., Cohen, A. S., ... and  
834 Slomp, C. P.: Ocean circulation in the Toarcian (Early Jurassic): a key control on deoxygenation and carbon  
835 burial on the European Shelf, *Paleoceanography and Paleoclimatology*, 33(9), 994 – 1012,  
836 <https://doi.org/10.1029/2018PA003394>, 2018.
- 837 Schweigert, G.: The occurrence of the Tethyan ammonite genus *Meneghiniceras* (Phylloceratina:  
838 *Juraphyllitidae*) in the Upper Pliensbachian of SW Germany, *Stuttgarter Beiträge zur Naturkunde Serie B*  
839 *Geologie und Paläontologie*, 356, 1 – 15, 2005.
- 840 Scott, A. C.: Charcoal recognition, taphonomy and uses in palaeoenvironmental analysis, *Palaeogeogr.*  
841 *Palaeoclimatol.*, 291(1 – 2), 11 – 39, <https://doi.org/10.1016/j.palaeo.2009.12.012>, 2010.
- 842 Sellwood, B. W., and Jenkyns, H. G.: Basins and swells and the evolution of an epeiric sea:(Pliensbachian–  
843 Bajocian of Great Britain), *J. Geol. Soc.*, 131(4), 373 – 388, <https://doi.org/10.1144/gsjgs.131.4.0373>, 1975.



- 844 Silva, R. L., Duarte, L. V., Comas-Rengifo, M. J., Mendonça Filho, J. G., and Azerêdo, A. C.: Update of the  
845 carbon and oxygen isotopic records of the Early–Late Pliensbachian (Early Jurassic, ~ 187 Ma): Insights from  
846 the organic-rich hemipelagic series of the Lusitanian Basin (Portugal), *Chem. Geol.*, 283(3–4), 177–184,  
847 <https://doi.org/10.1016/j.chemgeo.2011.01.010>, 2011.
- 848 Silva, R. L., Duarte, L. V., Wach, G. D., Ruhl, M., Sadki, D., Gómez, J. J., ... and Mendonça Filho, J. G.: An  
849 Early Jurassic (Sinemurian–Toarcian) stratigraphic framework for the occurrence of Organic Matter  
850 Preservation Intervals (OMPIs), *Earth Sci. Rev.*, 221, 103780, <https://doi.org/10.1016/j.earscirev.2021.103780>,  
851 2021.
- 852 Smith, P. L.: The Pliensbachian ammonite *Dayiceras dayiceroides* and early Jurassic paleogeography, *Can. J.*  
853 *Earth Sci.*, 20(1), 86–91, <https://doi.org/10.1139/e83-008>, 1983.
- 854 Steinhorsdottir, M., and Vajda, V.: Early Jurassic (late Pliensbachian) CO<sub>2</sub> concentrations based on stomatal  
855 analysis of fossil conifer leaves from eastern Australia, *Gondwana Res.*, 27(3), 932–939,  
856 <https://doi.org/10.1016/j.gr.2013.08.021>, 2015.
- 857 Storm, M. S., Hesselbo, S. P., Jenkyns, H. C., Ruhl, M., Ullmann, C. V., Xu, W., ... and Gorbanenko, O.:  
858 Orbital pacing and secular evolution of the Early Jurassic carbon cycle, *P. Natl. Acad. Sci. USA*, 117(8), 3974–  
859 3982, <https://doi.org/10.1073/pnas.1912094117>, 2020.
- 860 Suan, G., Mattioli, E., Pittet, B., Lécuyer, C., Suchéras-Marx, B., Duarte, L. V., ... and Martineau, F.: Secular  
861 environmental precursors to Early Toarcian (Jurassic) extreme climate changes, *Earth Planet. Sc. Lett.*, 290(3–  
862 4), 448–458, <https://doi.org/10.1016/j.epsl.2009.12.047>, 2010.
- 863 Suan, G., Nikitenko, B. L., Rogov, M. A., Baudin, F., Spangenberg, J. E., Knyazev, V. G., ... and Lécuyer, C.:  
864 Polar record of Early Jurassic massive carbon injection, *Earth Planet. Sc. Lett.*, 312(1–2), 102–113,  
865 <https://doi.org/10.1016/j.epsl.2011.09.050>, 2011.
- 866 Tappin, D. R., Chadwick, R. A., Jackson, A. A., Wingfield, R. T. R., and Smith, N. J. P.: *Geology of Cardigan*  
867 *Bay and the Bristol Channel, United Kingdom offshore regional report*, British Geological Survey, HMSO, 107  
868 pp, ISBN 0 11 884506 3, 1994.
- 869 Thibault, N., Ruhl, M., Ullmann, C. V., Korte, C., Kemp, D. B., Gröcke, D. R., and Hesselbo, S. P.: The wider  
870 context of the Lower Jurassic Toarcian oceanic anoxic event in Yorkshire coastal outcrops, UK, *Proceedings of*  
871 *the Geologists' Association*, 129(3), 372–391, <https://doi.org/10.1016/j.pgeola.2017.10.007>, 2018.
- 872 Thiry, M.: Palaeoclimatic interpretation of clay minerals in marine deposits: an outlook from the continental  
873 origin, *Earth Sci. Rev.*, 49(1–4), 201–221, [https://doi.org/10.1016/S0012-8252\(99\)00054-9](https://doi.org/10.1016/S0012-8252(99)00054-9), 2000.
- 874 Torsvik, T. H., and Cocks, L. R. M. (Eds.): *Jurassic*, in: *Earth History and Palaeogeography*, 208–218,  
875 Cambridge University Press, 2017.
- 876 Ullmann, C. V., Szűcs, D., Jiang, M., Hudson, A. J., and Hesselbo, S. P.: Geochemistry of macrofossil, bulk  
877 rock, and secondary calcite in the Early Jurassic strata of the Llanbedr (Mochras Farm) drill core, Cardigan Bay  
878 Basin, Wales, UK, *J. Geol. Soc.*, 179(1), <https://doi.org/10.1144/jgs2021-018>, 2022.



- 879 van de Schootbrugge, B., Bailey, T. R., Rosenthal, Y., Katz, M. E., Wright, J. D., Miller, K. G., Feist-Burkhardt,  
880 S., and Falkowski, P. G.: Early Jurassic climate change and the radiation of organic-walled phytoplankton in the  
881 Tethys Ocean, *Paleobiology*, 31, 73–97, [https://doi.org/10.1666/0094-8373\(2005\)0312.0.CO;2](https://doi.org/10.1666/0094-8373(2005)0312.0.CO;2), 2005.
- 882 van de Schootbrugge, B., Houben, A. J. P., Ercan, F. E. Z., Verreussel, R., Kerstholt, S., Janssen, N. M. M., ...  
883 and Suan, G.: Enhanced arctic-tethys connectivity ended the toarcian oceanic anoxic event in NW Europe, *Geol.*  
884 *Mag.*, 157(10), 1593 – 1611, <https://doi.org/10.1017/S0016756819001262>, 2019.
- 885 Waterhouse, H. K.: Orbital forcing of palynofacies in the Jurassic of France and the United Kingdom, *Geology*,  
886 27(6), 511 – 514, [https://doi.org/10.1130/0091-7613\(1999\)027<0511:OFOPIT>2.3.CO;2](https://doi.org/10.1130/0091-7613(1999)027<0511:OFOPIT>2.3.CO;2), 1999.
- 887 Weedon, G. P.: Hemipelagic shelf sedimentation and climatic cycles: the basal Jurassic (Blue Lias) of South  
888 Britain, *Earth Planet. Sc. Lett.*, 76(3 – 4), 321 – 335, [https://doi.org/10.1016/0012-821X\(86\)90083-X](https://doi.org/10.1016/0012-821X(86)90083-X), 1986.
- 889 Weedon, G. P., and Jenkyns, H. C.: Regular and irregular climatic cycles and the Belemnite Marls  
890 (Pliensbachian, Lower Jurassic, Wessex Basin), *J. Geol. Soc.*, 147(6), 915 – 918,  
891 <https://doi.org/10.1144/gsjgs.147.6.0915>, 1990.
- 892 Weedon, G. P., Jenkyns, H. C., and Page, K. N.: Combined sea-level and climate controls on limestone  
893 formation, hiatuses and ammonite preservation in the Blue Lias Formation, South Britain (uppermost Triassic–  
894 Lower Jurassic), *Geol. Mag.*, 155(5), 1117 – 1149, <https://doi.org/10.1017/S001675681600128X>, 2018.
- 895 Woodland, A. W. (Ed.): *The Llanbedr (Mochras Farm) Borehole*, Institute of Geological Sciences, London,  
896 Report No. 71/18, 115 pp., 1971.
- 897 Zakharov, V. A., Shurygin, B. N., Il'ina, V. I., and Nikitenko, B. L.: Pliensbachian-Toarcian biotic turnover in  
898 north Siberia and the Arctic region, *Stratigr. Geol. Correl.*, 14(4), 399 – 417,  
899 <https://doi.org/10.1134/S0869593806040046>, 2006.
- 900 Ziegler, P. A.: *Geological Atlas of Western and Central Europe*, 239, Shell Internationale Petroleum  
901 Maatschappij, The Hague, 1990.
- 902